Monthly Notices
of the
ROYAL ASTRONOMICAL SOCIETY

MNRAS **514,** 689–714 (2022) https://doi.org/10.1093/mnras/stac1267
Advance Access publication 2022 May 12

From dawn till disc: Milky Way's turbulent youth revealed by the APOGEE+*Gaia* data

Vasily Belokurov [1,2]★ and Andrey Kravtsov [3,4,5]★

[1] *Institute of Astronomy, Madingley Rd, Cambridge CB3 0HA, UK*
[2] *Center for Computational Astrophysics, Flatiron Institute, 162 5th Avenue, New York, NY 10010, USA*
[3] *Department of Astronomy and Astrophysics, The University of Chicago, Chicago, IL 60637, USA*
[4] *Kavli Institute for Cosmological Physics, The University of Chicago, Chicago, IL 60637, USA*
[5] *Enrico Fermi Institute, The University of Chicago, Chicago, IL 60637, USA*

Accepted 2022 May 3. Received 2022 May 3; in original form 2022 March 23

ABSTRACT

We use accurate estimates of aluminium abundance from the APOGEE Data Release 17 and *Gaia* Early Data Release 3 astrometry to select a highly pure sample of stars with metallicity $-1.5 \lesssim \mathrm{[Fe/H]} \lesssim 0.5$ born *in-situ* in the Milky Way proper. The low-metallicity ($\mathrm{[Fe/H]} \lesssim -1.3$) *in-situ* component we dub *Aurora* is kinematically hot with an approximately isotropic velocity ellipsoid and a modest net rotation. *Aurora* stars exhibit large scatter in metallicity and in many element abundance ratios. The median tangential velocity of the *in-situ* stars increases sharply with metallicity between $\mathrm{[Fe/H]} = -1.3$ and -0.9, the transition that we call the spin-up. The observed and theoretically expected age–metallicity correlations imply that this increase reflects a rapid formation of the MW disc over ≈1–2 Gyr. The transformation of the stellar kinematics as a function of [Fe/H] is accompanied by a qualitative change in chemical abundances: the scatter drops sharply once the Galaxy builds up a disc during later epochs corresponding to $\mathrm{[Fe/H]} > -0.9$. Results of galaxy formation models presented in this and other recent studies strongly indicate that the trends observed in the MW reflect generic processes during the early evolution of progenitors of MW-sized galaxies: a period of chaotic pre-disc evolution, when gas is accreted along cold narrow filaments and when stars are born in irregular configurations, and subsequent rapid disc formation. The latter signals formation of a stable hot gaseous halo around the MW progenitor, which changes the mode of gas accretion and allows development of coherently rotating disc.

Key words: stars: kinematics and dynamics – Galaxy: abundances – Galaxy: evolution – Galaxy: formation – Galaxy: stellar content – Galaxy: structure.

1 INTRODUCTION

The goal of Galactic archaeology is to unravel the physics of the high-redshift Universe by studying the close-by surviving relics of the early structure formation. The chain of events connecting the Cosmic Dawn era to the present day Milky Way can be investigated using low-mass stars with lifetimes of the order of the Hubble time and which thus bear witness to the first bouts of the early assembly of the Galaxy. The archaeological record is reconstructed by linking stellar elemental abundances and orbital properties whilst grouping stars by their chemical fingerprints, in the approach known as *chemical tagging* (see Freeman & Bland-Hawthorn 2002).

Eggen, Lynden-Bell & Sandage (1962) were the first to show how, with the help of galaxy evolution models, observed chemistry and kinematics of nearby stars can be interpreted to peer into the Milky Way's distant past. In their data set, a tight correlation appeared between stellar metallicity and orbital eccentricity. The metal-poor stars looked like they were on more radial orbits compared to the metal-rich ones which generally adhered to circular motion. However in a follow-up work, using a different observational sample, Norris, Bessell & Pickles (1985) pointed out that instead of a simple direct relationship between the orbital circularity and iron abundance, a less clear-cut picture likely existed. They revealed that metal-rich stars could show significant non-circular motions while metal-poor stars were allowed to follow the disc's rotation. Several decades later, the e-[Fe/H] plane has been mapped extensively with the help of wide-area sky surveys and shown to be filled with multiple overlapping populations whose exact nature remained unclear until recently (see e.g. Chiba & Beers 2000; Carollo et al. 2010).

Thanks to the arrival of the *Gaia* (Gaia Collaboration 2016) astrometric data together with large spectroscopic samples, some of the pieces of the Galactic puzzle have been deciphered. It was shown, for example, that the Milky Way's stellar halo contains contributions from multiple distinct sources. What had previously been considered a mixed halo 'field' can now be differentiated into: some material stripped from small satellites (Koppelman, Helmi & Veljanoski 2018; Myeong et al. 2018a,b,c; Koppelman et al. 2019; Naidu et al. 2020; Yuan et al. 2020; Malhan et al. 2022), copious amounts of tidal debris from a single massive dwarf galaxy (sometimes referred to as *Gaia*-Sausage or *Gaia* Enceladus, GS/E; see Belokurov et al. 2018; Deason et al. 2018; Haywood et al. 2018; Helmi et al. 2018; Mackereth et al. 2019), as well as many stars kicked out from the disc (Bonaca et al. 2017; Di Matteo et al. 2019; Gallart et al. 2019; Amarante, Smith & Boeche 2020; Belokurov et al. 2020).

★ E-mail: vasily@ast.cam.ac.uk (VB); kravtsov@uchicago.edu (AK)

Published by Oxford University Press on behalf of Royal Astronomical Society

Parallel to the charting of the Milky Way's stellar halo – generally represented by stars with low or negative angular momentum – significant focus has been on understanding the chemo-kinematic behaviour of the Galactic disc(s). In particular, the enigmatic extension of the so-called thick disc (Gilmore & Reid 1983) to low metallicities, dubbed the metal weak thick disc (MWTD), has been perplexing the community since the studies of Norris et al. (1985). While the follow-up analysis by Morrison, Flynn & Freeman (1990) appeared to confirm the earlier claims of Norris et al. (1985) as to the extension of the thick disc into the $-2 <$ [Fe/H] < -1 regime, questions were raised subsequently about possible biases in the photometric metallicities used in both studies (Twarog & Anthony-Twarog 1994; Ryan & Lambert 1995).

In this century, large spectroscopic samples, in particularly those procured by wide-area surveys have provided ample data to study the metal-poor wing of the thick disc. Taking advantage of vast numbers of freshly available spectroscopic metallicities, several independent studies reported an unambiguous detection of the thick disc stars at low iron abundances (see Chiba & Beers 2000; Beers et al. 2002; Carollo et al. 2010; Kordopatis et al. 2013; Li & Zhao 2017). Note however that typically in these pre-*Gaia* works, the MWTD is always identified as an additional contribution on top of the assumed halo component dominating the stellar number counts at low metallicities. Most recently, several groups used the *Gaia* astrometry together with spectroscopic or photometric metallicities to extend the detection of the disc population into very metal-poor regime (Sestito et al. 2019; Di Matteo et al. 2020; Fernández-Alvar et al. 2021). Surprisingly, stars with kinematics similar to both thick and thin disc are identified, reaching metallicities as low as $-6 <$ [Fe/H] < -3.

There are two observational obstacles to figuring out the exact lineage and the precise timeline of the Milky Way's evolution. First is the absence of high quality age measurements for truly old stars. Asteroseismological data to date remains scarce (see e.g. Grunblatt et al. 2021; Montalbán et al. 2021; Alencastro Puls et al. 2022), while the resolution of spectrophotometric ages deteriorates rapidly, increasing to 2–3 Gyr beyond 10 Gyr (see e.g. Hidalgo et al. 2011; Sanders & Das 2018). Secondly, even the very crude chemical tagging of stars into the 'accreted' and the 'born *in-situ*' categories starts to falter at old ages if only limited chemical information is available. This is simply because outside of the MW bulge, most old stars are metal-poor and would even have comparable α abundances because the α plateau is reached quickly at the onset of star formation. However, as we discuss below in Section 2.2, a much more robust identification of the *in-situ* component is possible using detailed chemical abundance measurements of the APOGEE survey, which serves as a foundation for this study.

Great strides in bringing observational picture of the Milky Way assembly into focus have been intertwined with significant improvements in understanding formation of disc galaxies in general (e.g. Naab & Ostriker 2017) and disc of the Milky Way specifically (e.g. Binney 2013). Much of the latter theoretical effort was dedicated to investigation of scenarios of the thick disc origin: from the first scenarios involving violent and turbulent early state of the Galaxy naturally leading to a fast formation of a hot disc component (Jones & Wyse 1983; Burkert, Truran & Hensler 1992; Brook et al. 2004; Bird et al. 2013, 2021) to formation of the thick disc by depositing stars (Abadi et al. 2003) and/or dynamical heating during mergers (see Quinn, Hernquist & Fullagar 1993; Velazquez & White 1999; Font et al. 2001; Hayashi & Chiba 2006; Kazantzidis et al. 2008; Villalobos & Helmi 2008).

At the same time, cosmological simulations of galaxy formation revealed that disc formation and evolution constitute an important, but relatively late stage of Milky Way's assembly. Two physically distinct regimes of gas accretion on to galaxies were identified in theoretical models: the 'cold flow' accretion mode, when gas accretes along warm filaments that can penetrate to the inner regions of haloes and a cooling flow mode wherein gas cools on to galaxy from a hot halo (Kereš et al. 2005, 2009; Dekel & Birnboim 2006; Dekel et al. 2009).

During early stages of evolution, when gas accretion is highly chaotic, progenitors of Milky Way-sized galaxies are expected to accrete gas via supersonic narrow filamentary flows. The chaotic accretion leads to irregular, highly turbulent, extended distribution of star forming gas and stars during early stages of star formation in Milky Way-sized progenitors (Rosdahl & Blaizot 2012; Stewart et al. 2013; Meng, Gnedin & Li 2019). It was also realized that feedback in simulations must be sufficiently strong to suppress star formation during these early epochs and prevent formation of massive stellar spheroid (e.g. Guedes et al. 2011; Hopkins, Quataert & Murray 2011, 2012; Agertz et al. 2013; Stinson et al. 2013; Vogelsberger et al. 2013; Crain et al. 2015). Strong stellar outflows and bursty star formation during early stages of evolution contribute to the overall chaos in the distribution of dense gas and star formation sites.

When halo mass and virial temperature become sufficiently large galaxies are able to sustain hot gaseous halo (Birnboim & Dekel 2003). Transition from the early chaotic stage of gas accretion to the slower accretion via cooling of gas from the hot halo or accretion is accompanied by 'virialization' of gas in the inner regions of halo and formation of coherent long-lived and coherently rotating gaseous disc via a cooling flow (Dekel et al. 2020; Stern et al. 2021). It is during this stage that the thin stellar discs in spiral galaxies form (Hafen et al. 2022).

In this study, we aim to probe the early chaotic stages of evolution of the main Milky Way's progenitor and transition to the build-up of the coherently rotating stellar disc. To this end, we use the APOGEE DR 17 data set (Section 2) and the available element abundances to identify a sample of stars that likely formed *in-situ* in the main progenitor (Section 2.2). We show that stellar kinematics and scatter in element abundances as a function of metallicity reveal a new low-metallicity *in-situ* stellar component that we associate with the early turbulent stages of Milky Way's evolution (Section 3). We also show the signature of the 'spin-up' of the Milky Way disc in the intermediate metallicity populations. We discuss and interpret observational results in Section 4 and summarize our results and conclusions in Section 6.

2 MILKY WAY *IN-SITU* STARS IN APOGEE DR17

In what follows we use aluminium to iron abundance ratios to differentiate between the *in-situ* and the accreted Milky Way populations following the ideas of Hawkins et al. (2015). Two aspects of [Al/Fe] evolution combine to help isolate the stars born in a massive galaxy with a rapid chemical enrichment. First is the metallicity dependence of the SN II Al yields (see Woosley & Weaver 1995; Nomoto, Kobayashi & Tominaga 2013). Secondly, similar to α-elements, is the dilution of [Al/Fe] with the increased output of SN Ia.

During early stages of evolution of the Galaxy when metallicity is small the Al output increases with increasing metallicity as more neutrons become available. While the comparatively massive Milky Way progenitor recycles the polluted gas efficiently and self-enriches quickly, the same process happens at a much more leisurely pace in a dwarf galaxy. The Milky Way enjoys a long enough phase of prolific [Al/Fe] growth before the SNe Ia start to contribute significantly. As a more relaxed dwarf reaches the necessary metallicity levels and starts to churn out Al, SNe Ia kick off and curtail the growth

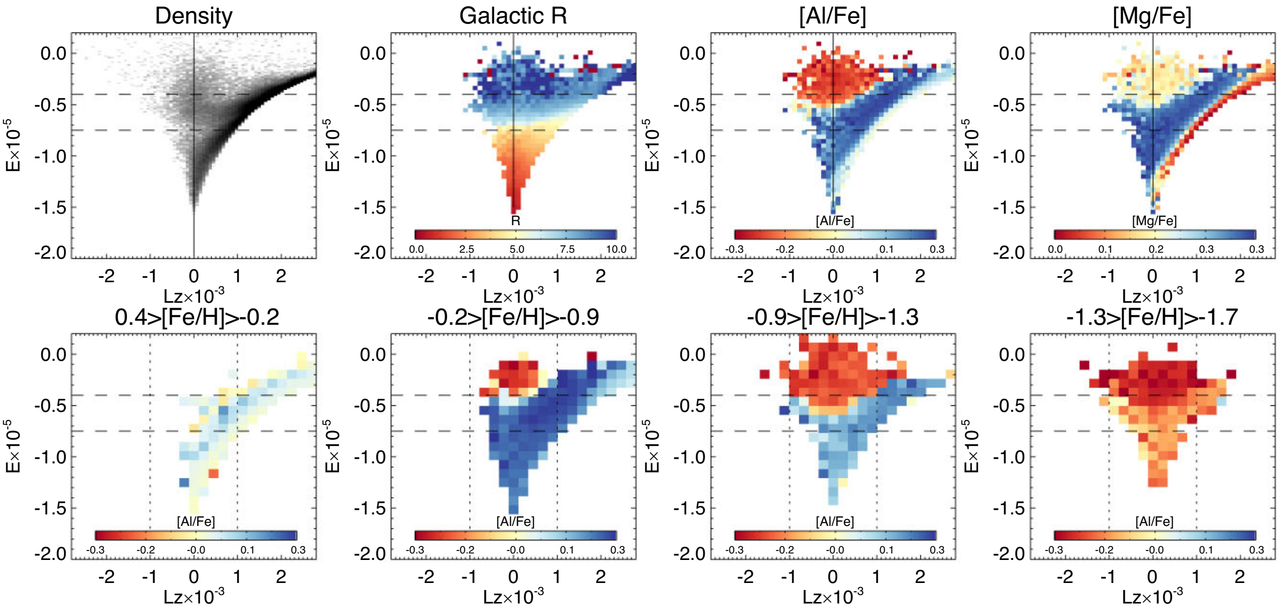

Figure 1. Distribution of ADR17 stars in the space of energy E and vertical component of angular momentum L_z. Top row, 1st panel: Logarithm of the stellar density. Note a noticeable horizontal gap at around $E \approx -0.75 \times 10^5$ corresponding the details of the ADR17 footprint. The two dashed horizontal lines show the energy restriction we apply for the subsequent analysis. Top, 2nd: Median Galactocentric radius. Note that the stars below the energy gap are located in the bulge region of the Milky Way, i.e. have $R < 3$ kpc. Top, 3rd: Median [Al/Fe]. Note a clear separation of the *in-situ* (high [Al/Fe] and accreted (low [Al/Fe]) populations. Top, 4th: Median [Mg/Fe]. The separation between *in-situ* and accreted is visible by the dynamic range is somewhat reduced. Bottom row E, L_z distribution coloured by [Al/Fe] in bins of iron abundance [Fe/H]. Bottom, 1st: Only the rotating disc is visible with intermediate [A/Fe]. Bottom, 2nd: Both accreted and *in-situ* populations are discernible thanks to very different [Al/Fe]. The *in-situ* stars display a low-L_z wing, known as Splash. Bottom, 3rd: While the typical [Al/Fe] for the accreted stars is the same at this metallicity, the mean [Al/Fe] of the *in-situ* population has decreased. Bottom, 4th: Even though the [Al/Fe] of the *in-situ* is reduced further, the accreted population can be easily identified since it has an even lower abundance of Al. Note that the shape of the *in-situ* distribution is now much more symmetric in L_z without a prominent rotating component.

of the [Al/Fe] abundance ratio. Therefore, in the analysis presented below, we view the behaviour of [Al/Fe] at $-2 <$ [Fe/H] < -1 as a basic but powerful indicator of rapid chemical enrichment. As such it is complementary to the classification based on α-elements used at higher metallicity (see e.g. Nissen & Schuster 2010; Hawkins et al. 2015; Hayes et al. 2018).

The broad-brush picture painted above has support in the literature. For example, Hasselquist et al. (2021) demonstrated that in the five most massive dwarf galaxies ever on orbit around the Milky Way, i.e. the Large and Small Magellanic Clouds (LMC and SMC), the Sagittarius, Fornax and the GS/E progenitor, median [Al/Fe] ratios do not exceed [Al/Fe] ≈ -0.2, while the Galactic disc stars exhibit significantly higher ratios of [Al/Fe] > 0. The difference in the Al enrichment between the Milky Way and smaller dwarfs was exploited to identify and study the likely accreted halo stars (e.g. Hawkins et al. 2015; Das, Hawkins & Jofré 2020; Horta et al. 2021). In contrast, in this study we use it to identify stars formed *in-situ* in the main progenitor of the Milky Way.

2.1 ADR17 Data

We rely on the data from the APOGEE Data Release 17 (ADR17; Abdurro'uf et al. 2022), more precisely the chemical abundance data is taken from the `allStarLite` catalogue available on the survey's website. The stellar Galactocentric coordinates, velocities, and integrals of motion as well as their uncertainties are taken from the AstroNN value-added catalogue (see Mackereth & Bovy 2018; Leung & Bovy 2019) which assumes the `MWPotential2014` gravitational potential from Bovy (2015). We choose to restrict the analysis to red giant stars with surface gravity estimates of $\log g < 3$ and velocity uncertainties of $<50\,\mathrm{km\,s^{-1}}$ in each of the three cylindrical velocity components. As we are interested in subtle chemical abundance trends, we also require uncertainty of <0.2 dex in the abundance estimates of the 9 elements, C, N, O, Mg, Al, Si, Mn, Fe, Ni, which ADR17 measures most reliably. We also eliminate stars with measurements suspected to be problematic, as signalled by the following flags: `STAR_BAD`, `TEFF_BAD`, `LOGG_BAD`, `VERY_BRIGHT_NEIGHBOR`, `LOW_SNR`, `PERSIST_HIGH`, `PERSIST_JUMP_POS`, `PERSIST_JUMP_NEG`, `SUSPECT_RV_COMBINATION`. Duplicate observations are removed by culling all objects with the fourth bit of `EXTRATARG` flag set to 1. Finally, we remove stars within 1 deg of any known Galactic satellite be it a dwarf galaxy or a globular cluster. We specifically remove stars in the Magellanic Clouds by eliminating all objects with `PROGRAMNAME` = `magclouds`. The totality of the above selection cuts leaves ≈214 000 stars.

Fig. 1 shows the distribution of the selected stars in the space of energy (E) and angular momentum (AM). The bulk of the stars in the sample pile up along the line of the maximal allowed AM. Also visible in the distribution of ADR17 stars is a horizontal gap around $E \times 10^{-5} \approx -0.75$ (see the leftmost panel in the top row of the figure). As already pointed out by e.g. Lane, Bovy & Mackereth (2021), this gap is due to the ADR17 footprint on the sky. There are crudely two distinct groups of pointings, one towards the Galactic centre and one sufficiently far away from it. The APDR17 selection function produces a bi-modal energy distribution. This is confirmed in the second panel of the top row where the colour-coding represents the median Galactocentric distance. As illustrated here,

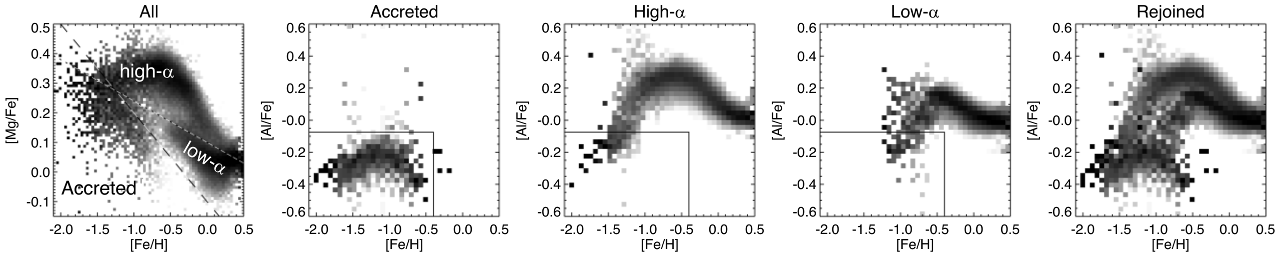

Figure 2. First panel: Column-normalized density of stars in the plane of [Mg/Fe] and [Fe/H]. The dashed and dotted diagonal lines show the selections for the ‘accreted’, ‘high-α’ and ‘low-α’ populations. 2nd: Column-normalized density of stars in the ‘accreted’ sample in the [Al/Fe] versus [Fe/H] plane. This sample is dominated by the GS tidal debris. The sequence shows a slow rise up to, followed by a decline and is in agreement with the GS pattern shown in Hasselquist et al. (2021). 3rd: Same but for high-α sample. 4th: Same but for the low-α sample. 5th: All three sequences added back together.

stars with energies $E \times 10^{-5} < -0.75$ typically reside within $\sim$3 kpc from the Galactic centre. For most of the analysis presented below we eliminate the ‘bulge’ contribution by removing stars with low energies (as indicated by the lower dashed horizontal line).

Panel 3 (4) in the top row of Fig. 1 shows the plane of energy and L_z, the vertical component of AM, colour-coded according to the median abundance of aluminium (magnesium) relative to iron. Both elements exhibit very clear separation between the stars formed *in-situ* and those formed in smaller progenitor galaxies and subsequently accreted on to the Milky Way. The accreted population typically shows a lower abundance ratio of [Al/Fe] and [Mg/Fe], although the magnesium-to-iron ratio also decreases in the thick disc due to increasingly large contribution of type Ia supernovae; [Mg/Fe] reaches the lowest values for the young stars in the thin disc at the highest metallcities probed. While both elemental ratios posses some discerning power, aluminium provides a larger dynamic range, in particular at low metallicities.

The ability of the [Al/Fe] to tell apart the accreted and the *in-situ* stars has been noticed before (see Hawkins et al. 2015) and is illustrated in the bottom row of Fig. 1. Here, as above, the $E - L_z$ plane colour-coded according to the median ratio of [Al/Fe] in each pixel but for four distinct bins of iron abundance, starting from super-Solar on the left and going to $\approx 0.02 Z_{\odot}$ on the right. Across the entire metallicity range considered, the *in-situ* stars are easily differentiated: they have higher [Al/Fe] ratio compared to the accreted population. Even for the stars at the lowest [Fe/H] considered, as shown in the fourth panel, this remains true. Indeed, the *in-situ* stars here can be seen as a funnel shape structure of lighter colour, corresponding to [Al/Fe] > -0.1, while the accreted population forms a higher energy pile mostly of maroon colour, with [Al/Fe] < -0.1.

2.2 *In-situ* selection

We take advantage of the discriminating ability of [Al/Fe] introduced above to build a sample of stars formed in the Milky Way across a wide range of metallicities. Fig. 2 helps us to elucidate the details of the [Al/Fe] behaviour of the individual components of the Galaxy as seen by ADR17 in the Solar neighbourhood (given the energy cut described above the bulk of the sample is within 3 kpc from the Sun). The figure connects familiar sequences in the [Mg/Fe]–[Fe/H] plane to their counterparts in the [Al/Fe]–[Fe/H] space. In the first panel, dashed and dotted diagonal lines are used to separate stars belonging to the accreted, the high-α and the low-α populations. These are then plotted in the subsequent panels.

The local accreted stars predominantly belong to a single merger event, namely the GES (see e.g. Belokurov et al. 2018; Iorio & Belokurov 2019). The accreted [Al/Fe] sequence (panel 2) shows a moderate rise up to $-0.2 <$[Al/Fe] < -0.1 at around [Fe/H] ≈ -1.2 followed by a decline. This pattern is entirely consistent with that presented in Hasselquist et al. (2021). The Milky Way’s high-α sequence (panel 3) rises much more rapidly with metallicity and as a result resides mostly above the accreted sequence across the entire range of [Fe/H]. Note that at [Fe/H] < -1.3 the high-α sequence dips below [Al/Fe] ≈ -0.1 and so at lower metallicities the *in-situ* stars start to overlap with the accreted population. The low-α sequence behaves in a similar fashion albeit offset in metallicity and [Al/Fe]: its rise is less steep and it does not reach as high levels of [Al/Fe] compared to the high-α sequence. After the turn-over around [Fe/H] ≈ -0.5, the two sequences are almost parallel meeting at super-Solar iron abundances. As the figure demonstrates, above [Al/Fe] ≈ -0.1, the contamination of the *in-situ* sample by the accreted debris is minimal.

Fig. 3 illustrates the details of the *in-situ* selection. To the selection cuts described above we add a restriction on the total energy (as given by the two horizontal dashed lines shown in Fig. 1, i.e. $-0.75 < E \times 10^5 < -0.4$) and a requirement that the heliocentric distance does not exceed 15 kpc. This reduces the sample to $\approx$79 500 stars. The leftmost panel 1 in the top row shows the column-normalized density of the selected stars in the plane of [Al/Fe] and [Fe/H]. Guided by the behaviour of local stellar populations shown in Fig. 2, two black lines demarcate the regions predominantly populated by the accreted and *in-situ* stars. All stars with [Fe/H] > -0.4 are deemed to be born in the Milky Way. Below this metallicity, we allocate stars with [Al/Fe] < -0.075 to the accreted population, while the *in-situ* stars have higher aluminium-to-iron ratios.

As a sanity check, we show the distribution of stars in the two samples of accreted and *in-situ* stars defined this way in the plane of [Mg/Fe]–[Fe/H] in the panels 2 and 3 of the top row of the figure. As panel 2 demonstrates, for $-1.5 <$ [Fe/H] < -0.5 the *in-situ* population remains on the alpha ‘plateau’, i.e. the increase in the iron abundance is accompanied by a constant Mg/Fe ratio. This can be contrasted with the evolution of magnesium in the sample of accreted stars. This relatively local sample is dominated by the tidal debris from the GES merger. The [Mg/Fe] track of the GES stars is very different from that of the stars born in the Milky Way’s main progenitor. In the range of metallicities considered, the GES-dominated halo population evolves to lower values of [Mg/Fe] with increasing iron abundance, starting the decline already at around [Fe/H] ≈ -1.3. This is a signature of significant SN Ia contribution to the Fe abundance and a symptom of a slower self-enrichment in a dwarf galaxy progenitor whose mass is significantly lower than that of the MW. This pattern is in perfect agreement with the earlier studies of the α abundance in the GS debris (see Haywood et al. 2018; Helmi et al. 2018; Mackereth et al. 2019).

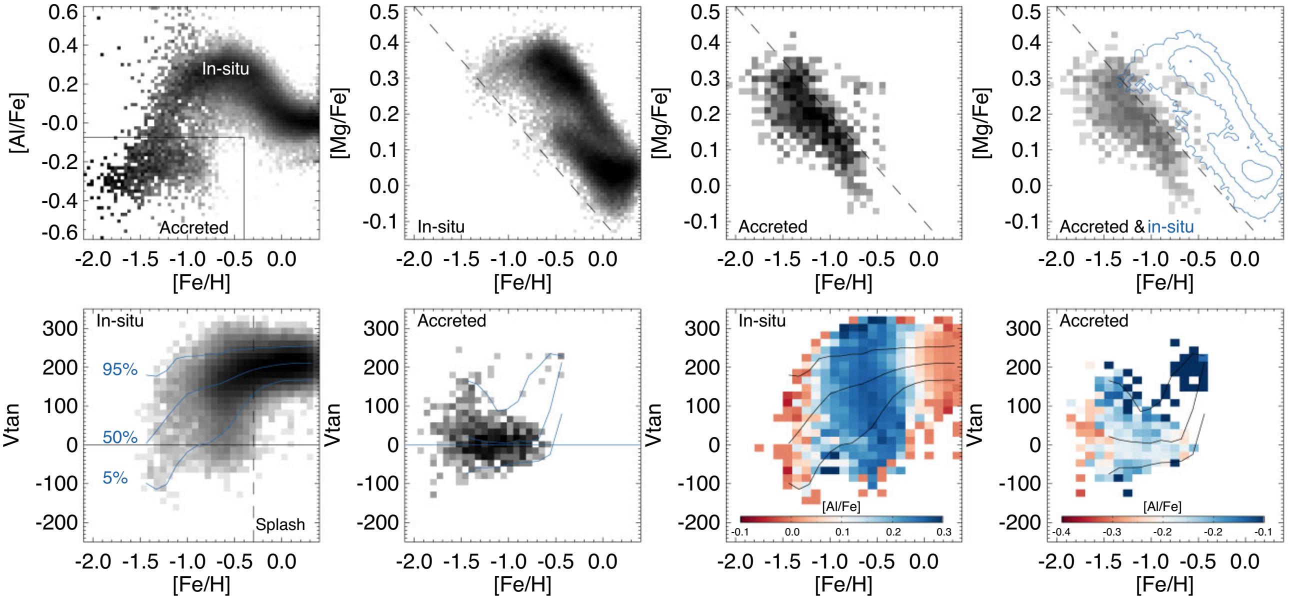

Figure 3. Separation of the *in-situ* and accreted populations. Top row, 1st panel: Column-normalized density of stars selected as described in Section 2.1 with the addition of the energy cuts illustrated in Fig. 1 in the space of [Al/Fe] and [Fe/H]. The solid black lines show the selection boundaries used to separate the stars born *in-situ* from those accreted on to the MW. Top, 2nd: Density distribution of the Al-selected *in-situ* population in the space of [Mg/Fe] and [Fe/H]. Top, 3rd: Same for the sample of accreted stars. Top, 4th: Both in-situ (contours) and accreted (greyscale density) populations are shown. The dashed diagonal line shows an addition cut used to clean the accreted population further. Bottom row, 1st panel: Logarithm of the density of stars in the plane spanned by azimuthal velocity $V_{\rm tan}$ and metallicity [Fe/H]. The solid curves gives the behaviour of the 5th, 50th, and 95th percentiles of the $V_{\rm tan}$ distribution as a function of [Fe/H]. Bottom, 2nd: Same but for the accreted stars. Note the difference in the behaviour of the $V_{\rm tan}$ distribution: at low [Fe/H] the *in-situ* distribution is broader with a rapidly increasing mode. The $V_{\rm tan}$ distribution of the accreted stars is narrow with approximately constant mode close to 0 km s^{-1}. Bottom, 3rd: The *in-situ* distribution colour-coded according to the median [Al/Fe] in each pixel. While a clear gradient of [Al/Fe] is seen with [Fe/H], at fixed metallicity no correlation is observed between $V_{\rm tan}$ and [Al/Fe], especially at [Fe/H] < -1. Bottom, 4th: Same for the accreted stars. Note that very high values of $|V_{\rm tan}|$ correspond to an increase of [Al/Fe]. We interpret this as a sign of contamination: some of the *in-situ* stars with low [Al/Fe] entered the accreted sample.

The bottom row of Fig. 3 demonstrates the chemokinematic behaviour of the two populations selected by [Al/Fe]. Specifically, the bottom row panels show the variation of the cylindrical azimuthal velocity component $V_{\rm tan}$ (equivalent to cylindrical V_ϕ) as a function of metallicity. First (leftmost) panel gives the density of *in-situ* stars in the plane of $V_{\rm tan}$ and [Fe/H] together with three lines corresponding to the run of the 5th, 50th, and 95th percentiles of the velocity distribution. According to the density distribution and confirmed by the behaviour of the velocity percentiles, the Milky Way possessed very little coherent spin at the epoch corresponding to the metallicity of [Fe/H] $\lesssim -0.9$. The median azimuthal velocity of the *in-situ* population is built up from approximately $0 < V_{\rm tan} < 50$ km s^{-1} at [Fe/H] ≈ -1.5 to a substantial $\approx$150 km s^{-1} at [Fe/H] ≈ -0.9. In contrast, the accreted halo stars (mostly the GES debris) have $V_{\rm tan} \approx$ 0 km s^{-1} for the entire [Fe/H] range probed (note that here we apply an additional cut in the [Mg/Fe] plane shown in the top row in an attempt to clean the accreted sample of a small number of *in-situ* interlopers).

Note that the mode and the width of the distribution of azimuthal velocities of the accreted population is largely due to the GS progenitor. The dwarf's orbit probably experienced a rapid radialization (see an extensive discussion in Vasiliev, Belokurov & Evans 2022), thus depositing its stellar debris on orbits with a typical AM close to zero. The width of the $V_{\rm tan}$ velocity distribution is relatively narrow, i.e. $50 < \sigma_{\rm tan}({\rm km\ s}^{-1}) < 100$ corresponding to the total mass of the parent GES halo of $\lesssim 10^{11} M_\odot$. Curiously, for the accreted stars with $-1.5 <$ [Fe/H] < -1 an additional component with high $V_{\rm tan}$ is visible reaching azimuthal velocities in excess of 100 km s^{-1}. These peculiar and abrupt changes in the velocity distribution is the results of the contamination of the accreted sample by the low-metallicity *in-situ* stars. As Fig. 2 demonstrates the high-α sequence enters the accreted [Al/Fe] region around [Fe/H] ≈ -1.3. Although such prograde rotating stars could, in principle, be a relic of a satellite accreted nearly in the disc plane (e.g. Abadi et al. 2003), this is unlikely in this case as the stars with significant $V_{\rm tan}$ have also a relatively high [Al/Fe] ratio as we discuss below.

Signatures of potential cross-contamination between the samples of accreted and *in-situ* stars can also be explored in panels 3 and 4 of the bottom row of Fig. 3. Here, the velocity distribution as a function of metallicity is colour-coded according to the median [Al/Fe]. Panel 3 shows that while there is a global trend of [Al/Fe] as a function of metallicity in the *in-situ* stars, at fixed metallicity [Al/Fe] ratio does not appear to be correlated with the azimuthal velocity. This is not the case for the accreted stars shown in the panel 4 of the figure. The regions corresponding to the highest $V_{\rm tan}$ also show a clear increase in the [Al/Fe] (compared to the rest of the population). This is a clear sign of contamination of the accreted sample with a small number of *in-situ* stars. Their presence is easy to recognize at high positive azimuthal velocities, but it is also betrayed at high negative values of $V_{\rm tan}$ where a mild increase in [Al/Fe] can also be seen. This is likely because in the range of $-1.5 <$ [Fe/H] < -0.9 the *in-situ* population has a much broader azimuthal velocity dispersion compared to that of the accreted halo. As discussed above the accreted population's azimuthal velocity spread is constrained by the internal kinematics of the GS progenitor. As judged by the patterns revealed in panels 3 and 4 of Fig. 3, we conclude that while the accreted population is mildly contaminated at [Fe/H] < -1.3, there are no obvious signs of the *in-situ* sample contamination.

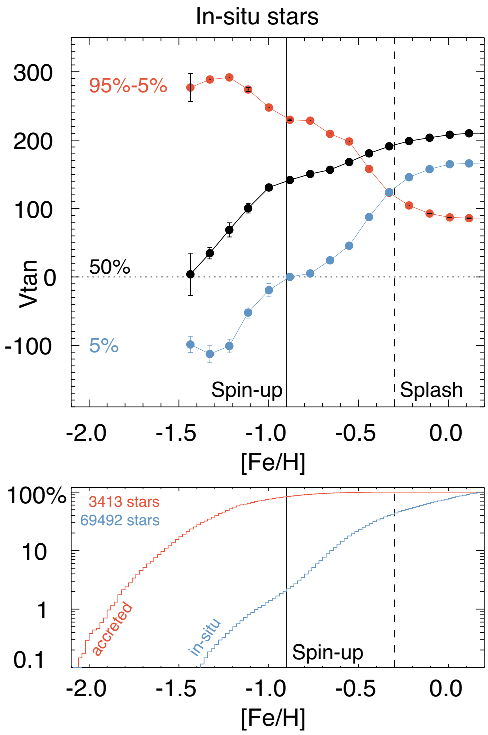

Figure 4. Top: Evolution of the *in-situ* azimuthal velocity distribution as a function of metallicity. The black curve and filled circles with error-bars give the change of the mode of the distribution, while blue and red showing the low-$V_{\rm tan}$ wing and the 3.3σ extent correspondingly. Culmination of the spin-up (Splash) phase is shown with a vertical solid (dashed) line. During the spin-up the overall spin of the *in-situ* stars is rapidly increasing, while the Splash is characterized by the emergence of the low-$V_{\rm tan}$ wing of the distribution. The bulk of the disc remains intact and spinning during and after the Splash. Bottom: cumulative metallicity distribution of the *in-situ* (accreted) sample is shown as the red (blue) histogram. Note the drastic difference between the two populations. At low [Fe/H], the *in-situ* sample is significantly depleted compared to the accreted one. This is indicative of a much faster and a more efficient star-formation activity in the MW progenitor at early times. By the time the spin-up phase was over, MW only formed ≈ 1 per cent of its stars. The accreted sample shows a slow-down above [Fe/H] ≈ −1.3 and truncation at [Fe/H] ≈ −0.5 corresponding to the epoch of the strong interaction between the GS progenitor and the MW.

3 THE EARLY MILKY WAY

3.1 Kinematics

Fig. 4 shows dependence of the kinematic properties in the Al-selected *in-situ* population as a function of metallicity, as well as fractions of stars in each sample at metallicity smaller than a given value. The curves corresponding to the 5th and 50th percentiles in the top panel are given to illustrate the change in the lowest and the typical AM population. This is complemented with the curve showing the difference between 95th and 5th percentiles representing the 3.3σ extent of the $V_{\rm tan}$ distribution. There are evident changes in the behaviour of the azimuthal velocity distribution as all three curves undergo marked transitions at two critical metallicities. Note that behaviour shown in the three curves is similar but not identical, which indicates that the alterations the Milky Way's kinematics incurred were non-trivial.

Before we delve into the details of the chemokinematic evolution of the Milky Way population, let us briefly compare the cumulative metallicity distributions of the stars born inside and outside the Milky Way. These are given in the bottom panel of the figure. At metallicities [Fe/H] < -1, the accreted stars dominate by almost >2 orders of magnitude.[1] This is because at this fixed metallicity we are peering further back into the past in the MW progenitor as it formed stars faster and self-enriched more efficiently than the GS/E progenitor. The small fraction of *in-situ* stars at low metallicities is qualitatively consistent with expectations of modern galaxy formation models, as we discuss in Section 4 (see Fig. 16). At [Fe/H] > -1, while Milky Way kept producing stars, the SF activity in the GES progenitor (the dominant contributor to the accreted sample) was stifled and quickly shut down as it interacted with the much bigger MW.

Let us follow the velocity curves from the metallicity just above [Fe/H] = 0, i.e. not too far from the present day, to lower [Fe/H], traversing Fig. 4 from right to left. This should approximately correspond to older stellar ages due to the observed metallicity–age relation (see e.g. Haywood et al. 2013; Feuillet et al. 2016, 2019; Silva Aguirre et al. 2018) as well as model expectations (see Section 4). Stars with $-0.3 <$ [Fe/H] < 0.2 reveal little change in their kinematics: all three curves are flat. The overall spin (black) is at its highest, $V_{\rm tan} > 200$ km s^{-1} (note that this is an average of the azimuthal velocities of the stars at different Galactocentric distances). The total (3.3σ) extent of the azimuthal velocity distribution is at its lowest, <100 km s^{-1} meaning that the average azimuthal velocity dispersion (red) is <30 km s^{-1}. The velocity distribution is tight around the peak: the lowest $V_{\rm tan}$ stars (blue) are only ∼30 km s^{-1} lower than those in the mode of the distribution. This is the recently formed portions of the Milky Way disc: kinematically cold and spinning fast.

The first dramatic transition happens at [Fe/H] ≈ −0.3. The low AM wing of the distribution quickly stretches to lower velocities; it decreases by a factor of 2 at [Fe/H]∼−0.5 and finally reaches 0 km s^{-1} at [Fe/H] ≈ −0.75. The expansion of the low-$V_{\rm tan}$ side of the distribution is reflected in the growth of the overall spread, which changes from ∼100 km s^{-1} at [Fe/H] ≈ −0.3 to ∼200 km s^{-1} at [Fe/H] ≈ −0.7. Note that the creation of a noticeable low-AM wing is not accompanied by a strong decrease in the typical spin of the Galaxy. Over the same range of metallicity, i.e $-0.7 <$ [Fe/H] < -0.3, the median $V_{\rm tan}$ decreases only by ∼50 km s^{-1}. The stretching of the velocity distribution towards low and even negative azimuthal velocities at intermediate iron abundances has been noticed before. The lowest AM stars are attributed to the so-called *in-situ* stellar halo (see e.g. Bonaca et al. 2017; Gallart et al. 2019). This structure is hypothesized to have been created by heating and splashing of the existing Milky Way disc as it interacts with the GES progenitor galaxy (see Di Matteo et al. 2019; Belokurov et al. 2020; Grand et al. 2020; Dillamore et al. 2022).

Then after a brief lull at $-0.9 <$ [Fe/H] < -0.7 where all three curves flatten, the second metamorphosis occurs between [Fe/H] ≈ −1.5 < and [Fe/H] ≈ −0.9. The most remarkable change is reflected in the behaviour of the Galactic spin: at the lowest of the metallicities considered i.e. [Fe/H] ≈ −1.5, no significant net rotation is present. This is also the epoch where the most substantial retrograde population is recorded together with the widest spread in azimuthal velocities. The change from no spin to a fast rotation happens rather quickly with increasing metallicity: by [Fe/H] ≈ −0.9

---

[1] Note that the *in-situ* sample's metallicity distribution is truncated at [Fe/H] < -1.5 due to the [Al/Fe] cut applied. This selection bias does not affect the overall differences between the distributions as described here.

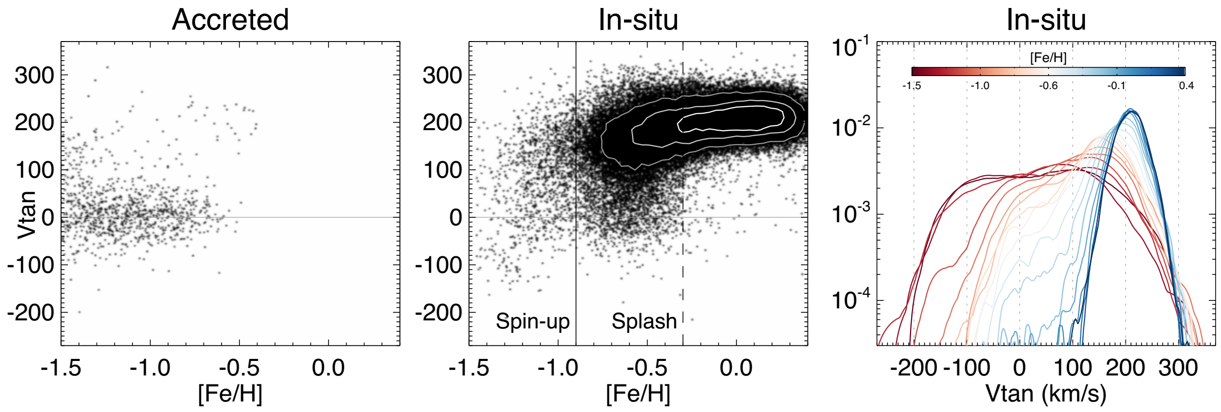

Figure 5. Azimuthal velocity V_{tan} as a function of metallicity. Left-hand panel: Stars identified as accreted using [Al/Fe]. This sample is dominated by the GS debris with the median spin near zero and a narrow range of V_{tan}. Note the clear contamination at [Fe/H] < -1.3 from the *in-situ* stars (see also Fig. 2). Middle: Scatter plot of the *in-situ* stars. Right-hand panel: KDE (with Epanechnikov kernel of optimal size) estimates of the probability density function of V_{tan} in bins of [Fe/H]. Note the low net spin and the wide span of the *in-situ* azimuthal velocity distributions at low metallicities.

the Milky Way's typical V_{tan} is already $\approx$150 km s^{-1}. Note that while the changes in the 5th and the 50th percentiles are also fast and striking, the evolution of the spread of the V_{tan} distribution is milder. As the Galaxy spins up, the spread tightens slowly: it only drops by less than 20 per cent, from $\approx$300 km s^{-1} to $\approx$250 km s^{-1} as the metallicity increases from -1.5 to -0.9. None the less, the azimuthal velocity distribution is at its wildest when $-1.5 <$ [Fe/H] < -1.3: the 3.3σ interval covers at least 300 km s^{-1}.

Fig. 5 provides additional details of the change in the V_{tan} distribution with metallicity. Azimuthal velocities of individual stars are shown as a function of [Fe/H] for the Al-selected *in-situ* population in the middle panel. At the lowest metallicities probed no obvious disc population can be detected. Note however that given the simple [Al/Fe] cut applied, many of the genuine *in-situ* stars with [Fe/H] < -1.3 will be a part of the accreted sample. This is indeed the case as shown in the left-hand panel of the figure: at [Fe/H] < -1.3 the V_{tan} distribution for the accreted sample suddenly becomes broader, including many stars with $V_{\mathrm{tan}} > 100$ km s^{-1}. The right-hand panel of Fig. 5 presents V_{tan} probability distribution functions for small bins of [Fe/H]. These pdfs are obtained using kernel density estimation (KDE) with Epanechnikov kernel of optimal size. The pdfs corresponding to the lowest metallicity bins are very broad, spanning $\approx$500 km s^{-1} from 200 to 300 km s^{-1}. The figure emphasizes that the spin-up, i.e. the change from a broad distribution with little net spin to a much slimmer peak centred on a $V_{\mathrm{tan}} > 100$ km s^{-1} happens over a narrow metallicity range.

The velocity ellipsoid of the *in-situ* stars with $-1.5 <$ [Fe/H] < -1.3 appears isotropic, i.e. $\sigma_z \approx \sigma_R \approx \sigma_\phi$, with all three dispersions in the range of 80–90 km s^{-1}. This is distinct from the 3D velocity distributions of both the GES debris and the Splash. The GES radial velocity dispersion is twice as high, in the range of 170–180 km s^{-1}. In the Splash, the azimuthal dispersion is lower, around 50–60 km s^{-1} (Belokurov et al. 2020).

The stars born in the Milky Way before it spins up, i.e. settles into a coherent disc provide a window into the earliest phases of our Galaxy's evolution. We therefore name this population *Aurora*, to symbolize the dawn of the Milky Way's formation. The *Aurora* and the Splash stellar populations correspond to the two junctures in the Milky Way's youth when rapid and consequential changes are unleashed. From the kinematic perspective, these two phases, that of formation and that of disruption, appear unconnected. The biggest give-away is the evolution of the spin: even though the interaction with the GS/E progenitor crumbles and disperses some of the existing stellar disc, the bulk of it remains intact retaining its relatively high rotational velocity. The creation of the Splash from the pre-existing disc also helps us to explain the difference in the amount of low- and negative V_{tan} stars during the two epochs. It is plausible to expect that a distinction between the *Aurora* and the Splash can also be drawn in the chemical dimension: the vastly different kinematic structure of the young Milky Way before and after disc formation may leave an imprint in the behaviour of key elemental abundances. In what follows we take advantage of the exquisite quality of the ADR17 data to examine chemical signatures of the spin-up and the Splash phases.

3.2 Chemistry

In order to make the chemical analysis more robust and to minimize the effects of any unwanted trends with stellar surface gravity and/or effective temperature, in this section we apply a stricter cut $\log g < 2$ to define stellar sample. Note that narrowing the range further to $1 < \log g < 2$ does not change any of the conclusions drawn below but increases the uncertainty.

3.2.1 Trends with [Fe/H]

Because several channels with distinct time-scales contribute to the production of iron, using Fe as a reference helps to emphasize temporal evolution of the star-formation and enrichment process.

Fig. 6 shows the metallicity dependence of the [X/Fe] abundance ratios for the eight chemical elements measured most reliably as part of the ADR17, namely: Al, Mg, Si, Ni, C, N, O, and Mn. These greyscale 2D histograms give column-normalized densities for the Al-selected sample of *in-situ* stars, or in other words, abundance ratio probability distributions conditional on [Fe/H]. In addition, blue solid (dashed) lines show the behaviour of the mode (5th and 95th percentiles) of the distribution. These can be compared to the median trends for the accreted population shown as the red solid curves.

The element abundance ratios of the *in-situ* stars display several clear trends. Around the metallicity of the Splash ([Fe/H] ≈ -0.3) two distinct sequences are visible at a given metallicity in all of the elements considered apart from N and Mn. The clearest separation between the high and the low abundance ratio branches can be seen in [Al/Fe], [Mg/Fe], [Si/Fe], and [O/Fe]. For stars with [Fe/H] < -0.3

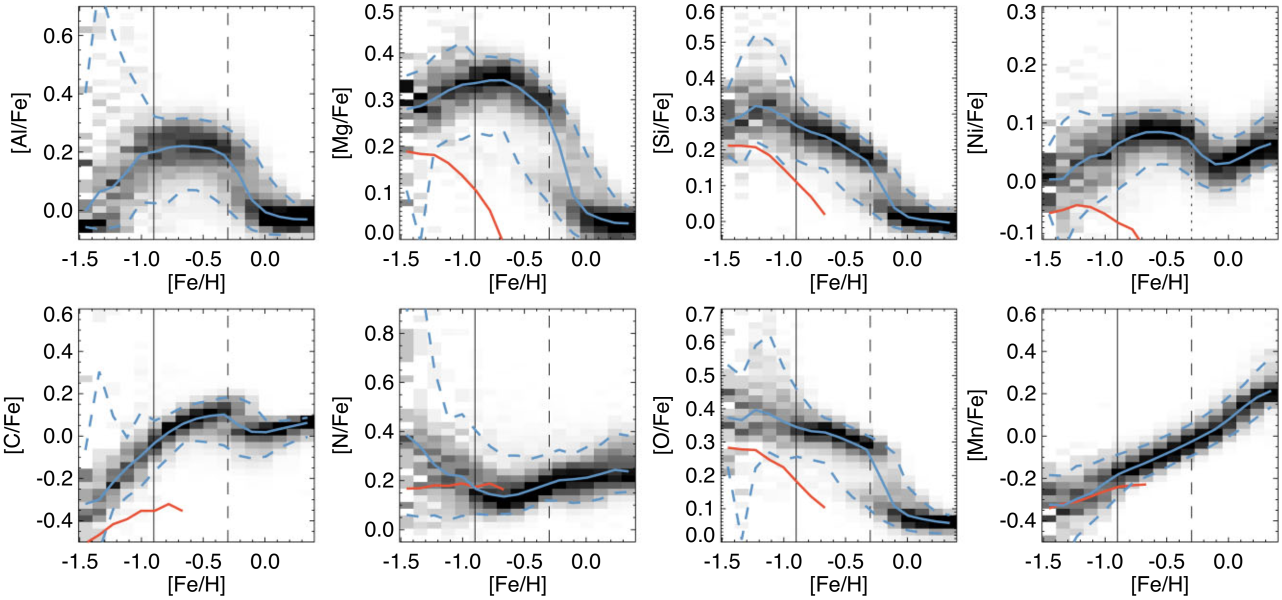

Figure 6. Column-normalized density of the distribution of the elemental abundance ratio [X/Fe] of the *in-situ* stars as a function of metallicity [Fe/H]. The blue (red) solid curve shows the median of the distribution of the *in-situ* (accreted) population. Additional cuts in energy $E \times 10^5 > -0.4$ and tangential velocity $|V_{\rm tan}| < 70$ km s^{-1} are applied to the accreted sample to minimize the contamination. The dashed blue curves show 5 per cent and 95 per cent of the *in-situ* distribution.

formed before the Splash, the upper branch (higher abundance at fixed [Fe/H]) is more populated, while for the stars with [Fe/H] > -0.3 the lower branch has the higher density. The accreted stars generally follow different trends in all elements. In all elements but N, the *in-situ* and the accreted abundance trends start to converge at the lowest metallicities. The [N/Fe] sequences are overlapping at around [Fe/H] ≈ -1 but are set apart by 0.1–0.2 dex at [Fe/H] $= -1.5$.

A standout feature of the abundance trends shown in Fig. 6 is the abrupt increase of the abundance spread at metallicities below [Fe/H] ≈ -0.9 (in several elements, the gradual uptick in dispersion happens at slightly higher metallicity, i.e. [Fe/H] < -0.7). As the figure demonstrates, many tight sequences that are consistently well-behaved at higher metallicities appear smeared or even completely destroyed below the threshold which we identified kinematically in the previous section. The most dramatic increases in the abundance dispersion at [Fe/H] < -0.9 are seen in [Si/Fe], [Ni/Fe], [N/Fe], and [O/Fe].

To investigate this phenomenon further, Fig. 7 shows the trends of the abundance distributions as a function of [Fe/H]. Here the median of the [X/Fe] abundance ratio (black) can be compared to the extent of the distribution (blue for *in-situ* and red for accreted stars, 3.3σ spread mapped by the difference between the 95th and the 5th percentiles). The behaviour of each element is shown as a band whose width gives the associated uncertainty (estimated using the bootstrap method). For the abundance dispersions we subtract the median of the reported uncertainties in quadrature. Note however that these uncertainties are extremely small (typically <0.05 dex across the entire metallicity range probed), as indicated by the black dotted lines that show 4 × the median uncertainty for each [Fe/H] bin.

Fig. 7 confirms that in all eight elements the spread in the abundance ratio of the *in-situ* population undergoes a dramatic change at [Fe/H] ≈ -0.9. At the same time, the median abundance track does not show any obvious large scale variations around the same metallicity in all elements but Al. Aluminium is shown to be sharply increasing up to [Fe/H] $= -0.9$ where it plateaus and stays constant until the contribution of type Ia supernovae starts to be noticeable at around [Fe/H] ≈ -0.5. The behaviour of the abundance spread for the Splash population is completely different: for stars with $-0.7 <$ [Fe/H] < -0.3 no strong abundance dispersion variation can be seen. Some minor spread increase is detectable but this is only because in the this metallicity range, two narrow sequences are present in many of the elements considered. Comparing the chemical signatures of the *Aurora* and the Splash, two distinct patterns are clear. The Splash stars share properties of the disc population, indicating their likely disc origin. At $-0.7 <$ [Fe/H] < -0.3, setting aside the apparent bi-modality of many of the elemental abundance ratios, the chemical enrichment sequences as reported by ADR17 are very narrow. Correspondingly, the 3.3σ abundance extent of the Splash stars is at the level of 0.1–0.2 dex. The elemental abundance spread in the stars born during the Spin-up phase is a factor of 2–4 larger. The cleanest example is nitrogen. Here no [N/Fe] bi-modality (i.e. existence of two standalone sequences at fixed [Fe/H]) is present at intermediate metallicities thus the abundance spread for stars with [Fe/H] $= -0.9$ is approximately constant at the level of 0.2 dex. The dispersion of [N/Fe] ratio grows sharply at lower metallicities reaching 0.8 dex at [Fe/H] < -1.3. Note that the median [N/Fe] also shows a mild increase (of the order of 0.2 dex) at low metallicities.

Based on their distinct chemical behaviour, as characterized by the extent of the abundance distribution, for the stars above and below [Fe/H] $= -0.9$ threshold we argue that the *Aurora* and the Splash populations are not connected. As we discuss in detail in Section 4, the low metallicity *in-situ* stars were not born in a disc and later dynamically heated, but had been born during the earlier Spin-up epoch under conditions sufficiently different from those that existed in a cold and fast-rotating disc later.

The overall extent shown in Fig. 7 gives an oversimplified illustration of the abundance ratio distribution as it does not indicate changes of its shape. As Fig. 6 demonstrates for many elements (e.g. [N/Fe] or [O/Fe]) the increase in the abundance ratio spread is clearly asymmetric. We explore the asymmetries in the distributions of chemical abundance ratios in the Appendix B. Fig. B1 studies the upper and

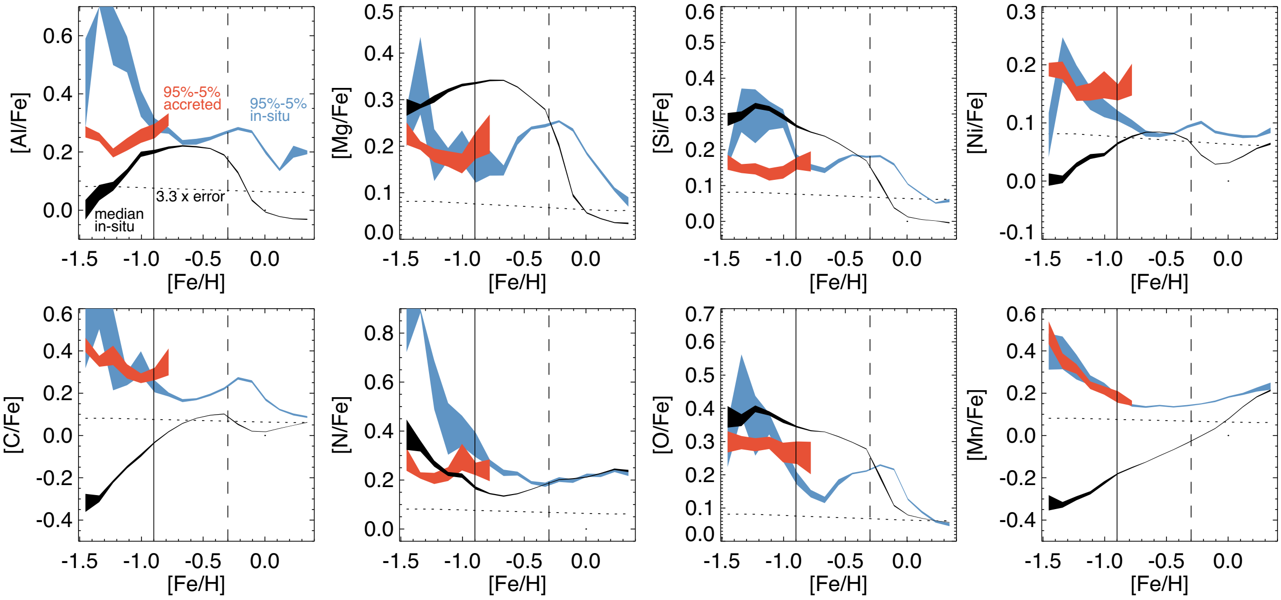

Figure 7. Statistics of the abundance ratio [X/Fe] distribution of the *in-situ* stars as a function of metallicity [Fe/H]. The width of the band shows the associated bootstrapped uncertainties. Black band is the median of the distribution, while the blue band gives the 3.3σ extent. For comparison, red band gives the abundance spread in the accreted population. The width of the abundance ratio distribution can be compared with the size of the ADR17 measurement uncertainty of the abundance ratio: dotted curve shows 3.3 times the measurement error.

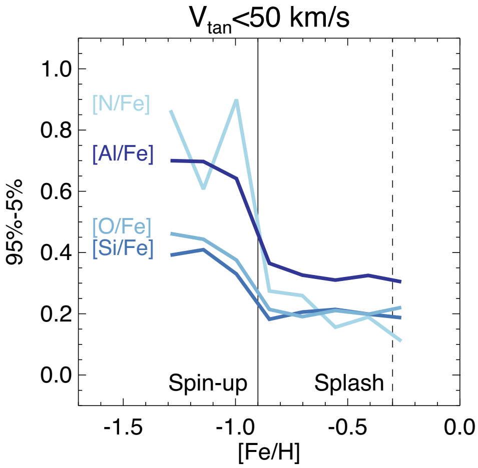

Figure 8. Evolution of the spread of the abundance ratio distribution of [Al/Fe], [Si/Fe], [N/Fe], and [O/Fe] as a function of metallicity for the *in-situ* stars with low or negative angular momentum, i.e. $V_{\rm tan} < 50$ km s^{-1}. At high metallicity this sample is dominated by the Splash population.

lower branches (with respect to the mode) of each of the [X/Fe] distributions separately. The figure confirms that at low metallicity, i.e. at [Fe/H] < -0.9, distributions of [Si/Fe], [N/Fe], and [O/Fe] become very asymmetric. In [Si/Fe] and [N/Fe] the bulk of the spread is upwards from the mode, while for [O/Fe] the behaviour of the two sides of the distribution appears to switch around [Fe/H] ≈ -1.3.

At high metallicity, i.e. [Fe/H] > -1, the distribution of the chemical abundance ratios of the *in-situ* population shown in Fig. 7 is dominated by the Galactic disc stars. This makes it difficult to assess whether the Splash population behaves differently from *Aurora* i.e. that born before (and during) the Spin-up phase. To clarify this, Fig. 8 displays the change in the abundance dispersion (as estimated by the 95 per cent–5 per cent difference) for the *in-situ* sample limited to retrograde stars only, i.e. to stars with $V_{\rm tan} < 50$ km s^{-1} (c.f. Belokurov et al. 2020). Here only the four elements that showed the increase in dispersion compared to the accreted populations are shown, namely Al, Si, N, and O. Notwithstanding the reduced number of stars, the picture remains the same. In fact, for the retrograde-only stars the behaviour is simplified: the metal-rich portion with [Fe/H] > -0.7 shows no bumps or wiggles, staying flat, while the increase in the width of the distribution at [Fe/H] < -0.9 is sharper.

3.2.2 *Trends with [Mg/H]*

Unlike iron, the Mg production is dominated by the core-collapse supernovae (CCSN). Thus, as pointed out by Weinberg et al. (2019), using Mg as a reference element greatly simplifies chemical enrichment trends (see also Wheeler, Sneden & Truran 1989; Cayrel et al. 2004; Hasselquist et al. 2021). For the elements mostly produced by CCSN, such as oxygen, abundance ratio relative to Mg stays constant if the yields are not metallicity-dependent. For odd-Z elements with metallicity-dependent yields, such as aluminum, the [X/Mg] ratio will steadily increase with [Mg/H]. For iron-peak elements, where multiple sources can contribute to the production (e.g. Fe), trends with [Mg/H] will be straighter compared to the trends with [Fe/H]. Overall, across all elements, trends of the abundance ratio [X/Mg] with [Mg/H] will look simpler, flatter, and less dependent on the details of the star-formation history.

To help relate the [X/Mg] abundance trends to the [X/Fe] ones discussed above, Fig. 9 shows the relation between [Mg/H] and [Fe/H]. Note that the relation is not one-to-one thanks to enrichment periods with multiple Fe sources in action. As a result, the threshold metallicity of [Fe/H] $= -0.9$ corresponds to a range of [Mg/H] values, namely $-0.7 <$[Mg/H] < -0.5. This leads to a blurring of the Spin-up kinematic transition discussed above, as illustrated in the right-hand panel of Fig. 9.

Fig. 10 shows the column-normalized density of stars in the space of [X/Mg] versus [Mg/H] similar to Fig. 6. In line with the ideas

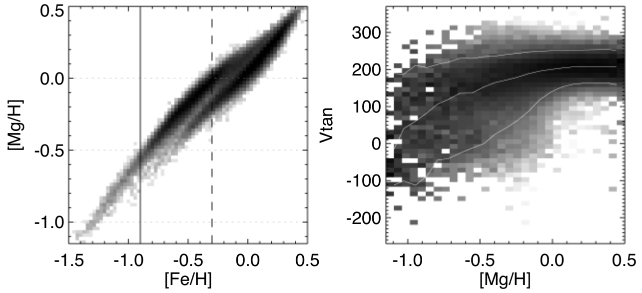

Figure 9. Left-hand panel: Magnesium abundance as a function of iron abundance. Logarithm of stellar density in the space of [Mg/H] and [Fe/H] is shown for the *in-situ* sample. Across a wide range of metallicity, at fixed [Mg/H], two values of iron abundance are possible thanks to the contribution of two iron sources, CCSNe and SNe Ia. Right-hand panel: Logarithm of column-normalized density in the space of azimuthal velocity and [Mg/H] for the *in-situ* sample. The white lines mark 5 per cent, 50 per cent, and 95 per cent of the $V_{\rm tan}$ distribution. At low [Mg/H] the transition for low $V_{\rm tan}$ to high $V_{\rm tan}$ is less sharp due to the increased contribution of the disc component at low [Mg/H].

discussed in Weinberg et al. (2019), most of the elemental abundance trends are significantly flatter, with the exception of C and N that show a larger amplitude of variation. Moreover, the abundance tracks of the *in-situ* and the accreted populations are much more alike, with the median curves lying close to (or on top of) each other. This includes Si, Ni, N, and O that previously showed unambiguously dissimilar behaviour. For Fe, Ni, and Mn, the accreted and the *in-situ* abundance tracks are offset thanks to a higher contribution of SN Ia at fixed metallicity in a dwarf galaxy environment compared to that in the Milky Way. Finally, the accreted population is some 0.1 dex lower in [Al/Mg] compared to the *in-situ*. We have checked that this is not an artefact of the selection (as the two populations are split on [Al/Fe]) and the difference persists if the accreted stars are selected using orbital information only. If Al was produced by CCSN only similar to Mg, we would expect similar levels of [Al/Mg] in the accreted and *in-situ* stars. Note that both Al and Mg are also produced by AGBs and in small quantities in SN Ia. Looking at the behaviour of other diagnostic elements dominated by either of these two sources, e.g. Ni for SN Ia and N for AGB, it is not clear that either could produce such an offset in [Al/Mg] between the accreted and *in-situ* populations.

As Fig. 11 demonstrates, not only the median tracks are flatter for some of [X/Mg] ratios (e.g. for Al and O), the spread increase towards lower metallicity is greatly reduced for the *in-situ* stars across all elements. For the accreted population, the abundance dispersion remains flat for all elements but N and O, likely due to the varying contribution of AGB stars. The relative reduction of the abundance spread when referenced to Mg makes sense: [X/Mg] ratios track the relative build up of metals while [X/Fe] fluctuates with rapid changes in gas accretion, star formation rate, and gas depletion time (e.g. Johnson & Weinberg 2020), as discussed in more detail in Section 4.5.

Comparison of the trends of scatter in the elemental abundance ratios referenced to Fe and Mg indicates that much of the increase in scatter at low metallicities is due to stochasticity of [Fe/H] due to the burstiness of the early star-formation histories of both the MW and the dwarf progenitor of the accreted population (see discussion in Section 4). Despite the simpler behaviour of [X/Mg] ratio trends, the increase of scatter in [Al/Mg], [Si/Mg], and [N/Mg] of the *in-situ* stars is still present at metallicities below the metallicities corresponding to the Spin-up stage of $-0.7 <$[Mg/H] < -0.5.

3.2.3 Similarities with chemical anomalies in star clusters

In the *in-situ* sample, the largest persistent (and systematically different from the accreted stars) increases of scatter of the element ratios at low metallicities are those displayed by Al and N. This behaviour is reminiscent of large chemical anomalies observed in stars in most of the Galactic globular clusters (GCs). Although very uniform in [Fe/H], GCs have turned out to have significant spreads in He, C, N, O, Na, and Al, with other elements such as Mg and

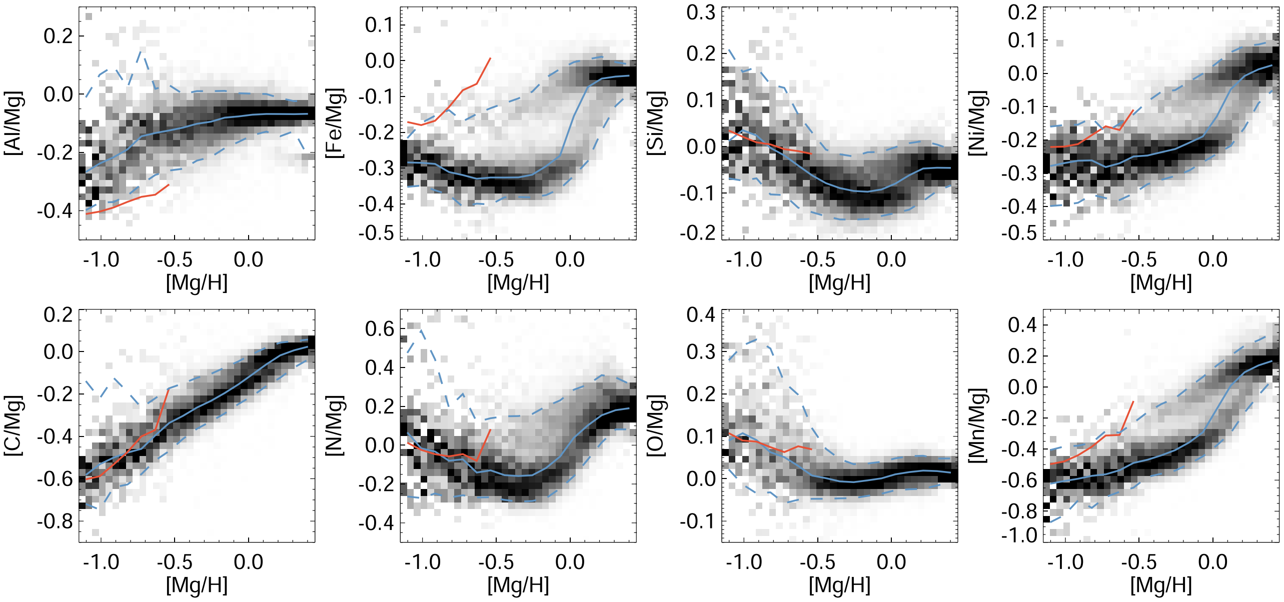

Figure 10. Same as Fig. 6 but for the evolution of the abundance ratios referenced to Mg. Note a flatter appearance of most tracks and a better match between the *in-situ* and the accreted populations.

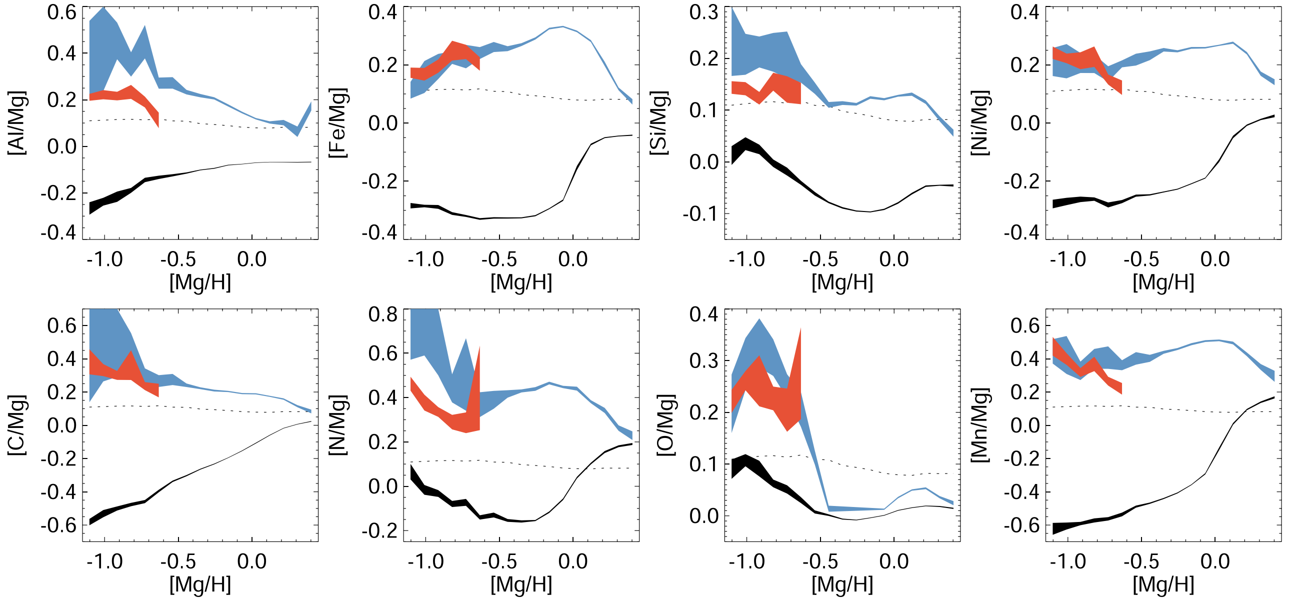

Figure 11. Same as Fig. 7 but for the evolution of the distribution of the abundance ratios referenced to Mg. Note the excess dispersion in [Al/Mg], [Si/Mg], and [N/Mg] at low [Mg/H].

Si also implicated, which indicate multiple star formation episodes during cluster formation (see Gratton, Sneden & Carretta 2004; Bastian & Lardo 2018, for review). Enrichment in some elements is facilitated by the consumption of others, e.g. N and Na are produced while C and O are depleted, leading to high-amplitude abundance (anti)correlations within a single GC. In some GCs, overproduction of Al, sometime by more than 1 dex, has been linked to the depletion of Mg, thus establishing strong Al-Mg anticorrelation (see e.g. Pancino et al. 2017; Masseron et al. 2019).

It is hypothesized that the necessary enrichment takes place in the interiors of the earlier generations (often referred to as the first generation or 1G) of the GC stars and the synthesized material subsequently pollutes the older generations (referred to as the second generation or 2G). As of today no clarity exists as to how and where exactly the synthesis happens (Renzini et al. 2015; Bastian & Lardo 2018). Some of the requirements may be very unusual: for example the transformation of Mg into Al necessitates extreme temperatures achieved in massive main sequence stars, in excess of 100 $M_\odot$ (see e.g. Prantzos, Charbonnel & Iliadis 2007, 2017; Denissenkov & Hartwick 2014) or potentially, AGBs (see Cottrell & Da Costa 1981). It is also unclear how exactly the products enriched by the 1G stars are delivered to their 2G siblings.

Moreover, instead of a well-defined trend, GCs exhibit a range of behaviours: for example, sometimes a correlation between Mg and Al is observed, sometimes it is not (e.g. Carretta et al. 2009; Pancino et al. 2017); in some clusters Al correlates with Si and in others it does not (e.g. Yong et al. 2005; Carretta et al. 2009; Masseron et al. 2019). However, it has been noted that the amplitude of the spread and the strength of the abundance correlation grows with the increasing cluster mass and decreasing metallicity (e.g. Carretta et al. 2010; Masseron et al. 2019). The metallicity dependence is particularly striking, instead of a smooth trend a discontinuity exists around [Fe/H] ≈ -1 below which the overall [Al/Fe] spread increases sharply (see e.g. Pancino et al. 2017).

Although no fully developed theory exists to explain the genesis of the chemical anomalies observed in the Galactic GCs, signatures of N and Al overabundance have been used to identify stars that may have belonged to massive star clusters in the past but are now in the field. In some of the most convincing implementations of the 'chemical tagging' idea, excess of N and Al (and sometimes Si) have all been used to single out former GC member stars in the field (see e.g. Martell et al. 2011, 2016; Lind et al. 2015; Schiavon et al. 2017; Koch, Grebel & Martell 2019; Fernández-Trincado et al. 2020).

Do the *in-situ* stars contributing to the excess Al, N, Si abundance spread at [Fe/H] < -0.9, i.e. in the *Aurora* population and during the Spin-up phase discussed earlier in this paper behave similarly to the stars born in the Galactic GCs? Fig. 12 provides an answer to this question by exploring possible correlations in abundance ratios of the MW stars with $-1.5 <$ [Fe/H] < -0.8. Focusing on the behaviour of the Al abundance shown in the top row, at least three groups of stars with distinct properties can be identified. First, there are the clear outliers – the stars with [Al/Fe] > 0.4 that exhibit a correlation with [N/Fe] and an anticorrelation with [Mg/Fe] and [O/Fe]. These stars, mostly limited to [Fe/H] < -1.3, display exactly the chemical signatures observed in the MW GCs. Extreme in some of the chemical properties this group is rather small, counting a dozen or so objects. A second slightly bigger group with a somewhat higher metallicity and with lower values of [Al/Fe] on average (but still in excess of [Al/Fe] > 0.4) shows a different behaviour: no clear correlation between Al and N, as well as the absence of anticorrelation between Al and Mg, O. This group shows a positive correlation between Al and Si, with an excess of [Si/Fe] > 0.4. Finally, the third group comprising the bulk of the low metallicity stars has [Al/Fe] < 0.4 and lower values of [Si/Fe] < 0.4. This group shows weaker but still discernible correlations between Al and Si, C and N, O and C.

The first two groups contribute the most to the increase of the abundance dispersion at [Fe/H] < -0.9 in Al and Si. In particular, the first group with the chemical trends most in agreement with the observed GC anomalies contains the highest Al (as well as Mg and O) outliers. Note that even if these stars are removed, the dispersions in [Al/Fe] and [Si/Fe] remain anomalous at [Fe/H] < -0.9. However removing the stars from both the first and the second group removes

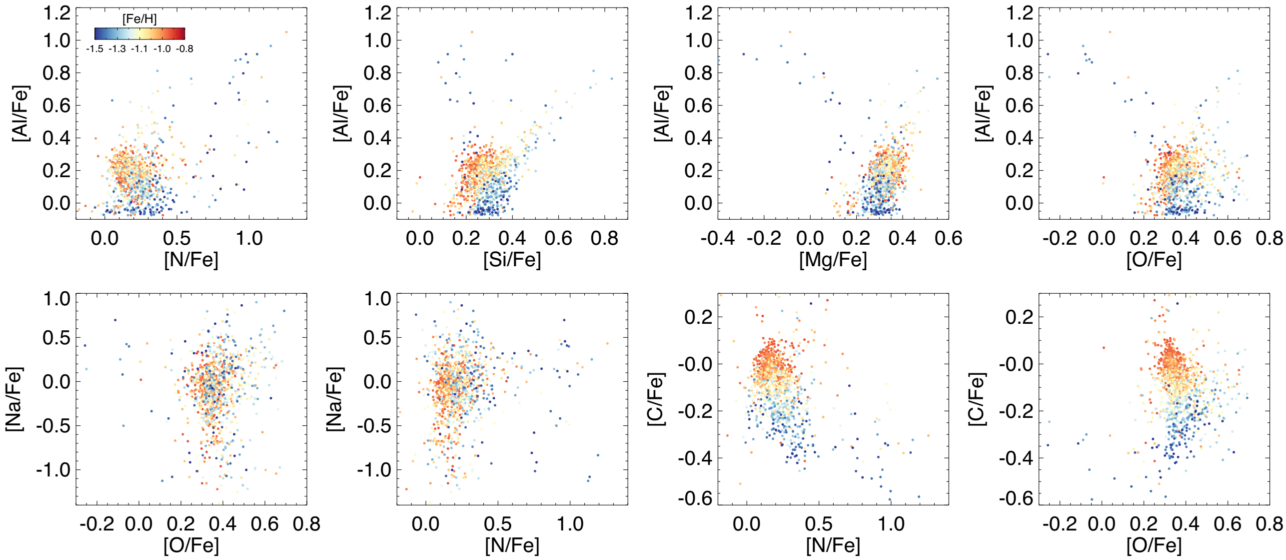

Figure 12. Abundance ratio correlations for the *in-situ* stars with $-1.5[\mathrm{Fe/H}] < -0.8$. The data-points are colour-coded according to their metallicity. At low metallicity, three groups with distinct Al behaviour are noticeable. First, a small group of high [Al/Fe] outliers, showing correlation with [N/F] and anticorrelation with [Mg/Fe] and [O/Fe]. Secondly, slightly larger group with [Al/Fe] values lower than the first but still in excess of [Al/Fe] > 0.4. These stars show a correlation between [Al/Fe] and [Si/Fe]. Finally the third group has [Al/Fe] < 0.4 and exhibiting correlations between C and N, as well as between C and O. The N dispersion of this group is reduced compared to the high Al, N outliers but is still substantial.

the increase of scatter in [Al/Fe] and [Si/Fe] entirely. The increase of scatter in [N/Fe], however, persists as it is driven by the stars from the third (most numerous) group, with relatively low N abundances (as demonstrated by the top left-hand panel of Fig. 12. The bottom row of the figure also shows the behaviour of Na as a function of O and N. Unfortunately, no clear pattern can be detected, due to the relatively low quality of Na measurements in ADR17 at this level of [Fe/H]. The last two panels show the behaviour of C, N, and O, and confirm the patterns identified above.

To conclude, only a small fraction of stars, namely those in the first group discussed above (largest Al and N abundances), show unambiguously the behaviour consistent with the GC origin. Note however that the fractional contribution of these stars increases sharply below the metallicity $[\mathrm{Fe/H}] \approx -1$ and drives the excess dispersion in [Al/Fe]. This sharp metallicity dependence is very similar to the pattern displayed by anomalous stars in the Galactic GCs (e.g. Pancino et al. 2017) and in the field (see e.g. Schiavon et al. 2017). Moreover, given the diversity of the chemical behaviour observed in the Galactic GCs we cannot rule out that stars in group two, and even in group three, experienced enrichment linked to massive star cluster evolution.

4 EARLY EVOLUTION OF THE MILKY WAY: CLUES FROM GALAXY FORMATION MODELS

4.1 Two regimes of gas accretion on to galaxies and disc formation

Although many aspects of galaxy formation are still not fully understood and remain a subject of active research and debate, studies over the last three decades have helped us to understand the key stages in galaxy evolution. In particular, two physically distinct regimes of gas accretion on to galaxies were identified: the ‘cold flow’ filamentary mode, in which gas accretes along warm filaments that can penetrate to the inner regions of haloes and a cooling flow mode wherein gas cools on to galaxy from a hot halo (Kereš et al. 2005, 2009; Dekel & Birnboim 2006; Dekel et al. 2009). Physically, the regime of accretion is determined by the ability of a system with a given metallicity and halo mass to maintain a hot halo (Birnboim & Dekel 2003).

During early stages of evolution, when gas accretion is highly chaotic, progenitors of Milky Way-sized galaxies accrete gas via fast flows along narrow filaments with large angular momentum that is often oriented differently for different flows (Pichon et al. 2011; Stewart et al. 2011; Sales et al. 2012; Danovich et al. 2015). This leads to irregular, highly turbulent, extended distribution of star forming gas and stars during early stages of star formation in Milky Way-sized progenitors (Rosdahl & Blaizot 2012; Stewart et al. 2013; Meng et al. 2019).[2]

Stars formed during the early chaotic stages of evolution dominated by cold flow accretion will not be distributed in a thin coherently rotating disc, but in a spheroidal or a very thick disc configuration (Bird et al. 2013, 2021; Obreja et al. 2013, 2019; Yu et al. 2021). As shown explicitly by Meng & Gnedin (2021), for example, even if stars are forming in gas with a flattened rotating gas configuration at a given time at high z, the disc rapidly changes orientation (see also McCarthy et al. 2012; Tillson et al. 2015; Kretschmer, Dekel & Teyssier 2022) or gas distribution changes to a completely non-disc configuration during subsequent epochs. Likewise, even when stars are forming in a thick perturbed disc at high z, the subsequent fluctuations of potential due to mergers and high degree of variability in mass accretion and/or feedback-driven outflows lead to rapid relaxation and spheroidal stellar distribution

---

[2] Qualitatively, this picture is a robust prediction of the Cold Dark Matter scenario and is not sensitive to details of galaxy formation physics (e.g. Stewart et al. 2017), although whether or not the filaments penetrate all the way to discs may depend on numerical effects and proper treatment of relevant instabilities during supersonic gas flows (e.g. Mandelker et al. 2019, 2020, 2021).

(Kazantzidis et al. 2008, 2009; McCarthy et al. 2012; Bird et al. 2013; Dekel et al. 2020; Tamfal et al. 2022). Thus, due to the entirety of these factors, during early high-rate accretion stage of evolution most progenitors of the Milky Way mass galaxies cannot form or maintain a thin disc.

This is illustrated in Fig. 13, which shows spatial distributions of stellar particles younger than 100 Myr at $z = 4$ and $z = 3$ and distribution of the same particles at $z = 0$ in four representative MW-sized galaxies from the FIRE-2 Latte simulations suite. The figure shows a chaotic distribution of young stars forming at $z = 4$ and $z = 3$, before the disc appeared in each object, while the right-hand column shows that orbital mixing and relaxation result in spheroidal distribution of these stars around galactic centre at the present epoch. Note that if needed conversion between redshift and look-back time or stellar age can be approximately made using the upper axis that shows z at the corresponding ages.

When halo mass and virial temperature become sufficiently large, shock-heated gas does not cool as fast as during early stages and hot gaseous halo can exist (Birnboim & Dekel 2003). Emergence of such hot halo around the disc results in transition from the early chaotic stage of gas accretion along cold narrow filaments to the slower accretion via cooling of gas from the hot halo or accretion of gas stripped from satellites. This transition is accompanied by 'virialization' of gas in the inner regions of halo and formation of a coherent long-lived and coherently rotating gaseous disc via a cooling flow (Dekel et al. 2020; Stern et al. 2021). It is during this stage that the thin stellar discs in spiral galaxies form (Hafen et al. 2022). The process of transition from the early chaotic distribution of gas to coherently rotating, persistent disc was explicitly studied in the FIRE simulations in a recent study by Gurvich et al. (2022).

The scenario outlined above is consistent with statistical results of Pillepich et al. (2019), who used the TNG50 simulation of a $\approx$50 Mpc box to show that statistically galaxies with disc morphologies in gas and stellar distributions emerge only at redshifts when galaxies have halo masses sufficiently massive to maintain hot halo. For example, their Figs 8 and 9 show that disc morphologies dominate at $z \leq 4$ in galaxies with $M_\star > 10^{10}\,M_\odot$, which occupy haloes of mass $M_{\rm h} \gtrsim 5 \times 10^{11}\,M_\odot$ (e.g. Behroozi, Wechsler & Conroy 2013). These masses, however, are much higher than the expected mass of MW progenitors at these redshifts. In lower mass haloes, however, distribution of gas and stars is predominantly spheroidal.

4.2 Evolution of stellar mass, metallicity, and star formation rate in progenitors of MW-sized galaxies

General implication of galaxy formation models outlined above is that formation of a thin coherently rotating disc in galaxies, such as the Milky Way, is expected to coincide with formation of the inner hot gaseous halo at relatively late stages of evolution $z \lesssim 1$–2. It is thus tempting to identify the transition from the chaotic velocity distribution with $\overline{V}_{\rm tan} \approx 0$ at [Fe/H] $\lesssim -1$ to large $V_{\rm tan}$ at higher metallicities in the observations discussed above with that stage. The metallicity of [Fe/H] $\lesssim -1$, is lower than the metallicity of the 'Splash' stars, and so dates from the epochs before the merger with the GS/E galaxy. Given that precise stellar ages are not available in observations, we can gauge the typical expected range of ages for stars with [Fe/H] $\lesssim -1$ using theoretical models.

Fig. 14 shows evolution of halo mass defined within the density contrast 200 times the critical density, as well as the metallicity–age relation for stars and evolution of star formation rate for a sample of galaxies forming in Milky Way-sized haloes in the GRUMPY regulator model (Kravtsov & Manwadkar 2021) using mass accretion histories from the ELVIS suite of dark matter simulations (Garrison-Kimmel et al. 2014), and cosmological zoom-in N-body+hydrodynamics simulations of several Milky Way-mass galaxies from the FIRE-2 simulation public data release[3] (Wetzel et al. 2022),[4] as well as the Auriga simulations available in the Aurigaia public release (Grand et al. 2018).[5] Note that we only plot the '*in-situ*' stars in all models: in the GRUMPY model only such stars are modelled for each host, in the FIRE simulations we only use star particles formed at less than 30 comoving kpc from the progenitor centre at each epoch, and in the Auriga simulations we use the *in-situ* flag provided with the data release to select stellar particles. In both the FIRE and Auriga simulations we select stars with $5 < R/{\rm kpc} < 11$ and $|Z| < 3$ kpc. In addition, to calibrate the metallicity distribution to the Milky Way and bring different simulations to a common metallicity scale, we shift stellar metallicities of the selected stars by a constant factor so that their median metallicity equals to the solar value, in agreement with the median metallicity of stars in the Milky Way at these radii (e.g. Katz et al. 2021). This shift is small: $\approx$0.05–0.1$Z_\odot$ for the Auriga and $\approx$0.01–0.3$Z_\odot$ for the FIRE objects (with the most typical shifts of 0.1–0.2).

The galaxy evolution models considered here all result in galaxies with realistic properties at $z \approx 0$, but they are very different in how they model galaxy formation. Comparison of their results should therefore give a reasonable estimate of the range of theoretical expectations.

The two regimes of fast and slow mass accretion separated by the look-back time of $\approx$11 Gyr are clearly visible in the evolution of $M_{\rm 200c}$ in the top panel of Fig. 14. These two regimes are reflected in the two regimes of stellar mass buildup in the lower panel: an extremely fast rise of star formation rate at the look-back times of $\gtrsim$11 Gyr and a steady star formation rate at later epochs (on average, cf. also Ma et al. 2017; Flores Velázquez et al. 2021; Yu et al. 2021; Gurvich et al. 2022, for analyses of these two regimes in the context of stellar disc formation in the FIRE-2 simulations). In addition to the overall average behaviour of SFR(t) in these two regimes, the burstiness of star formation in the FIRE simulations is also very high during early stages of evolution and is much smaller during later stages after virialization of the inner hot halo and formation of the coherent gaseous disc (Stern et al. 2021; Yu et al. 2021; Gurvich et al. 2022; Hafen et al. 2022), as illustrated by the track of the `m12i` Latte run shown in the lower panel of Fig. 14. Note that in these simulations burstiness can remain substantial well past the overall transition between the two regimes in the average SFR. For example, in `m12i` this transition occurs at the look-back time of $\approx$10–11 Gyr, while star formation remains bursty to $\approx$4 Gyr and as a result thin disc in this simulation forms only at the look-back times $\lesssim$3.2 Gyr (see table 1 in Yu et al. 2021).

The metallicity of 0.1$Z_\odot$, however, is achieved much earlier than the epoch of disc formation in the model Milky Way-mass galaxies. Fig. 14 shows that in both the GRUMPY model results and in the Latte and Auriga simulations the stars with $Z \approx 0.1Z_\odot$ typically form at the look-back times $\approx 11 \pm 1$ Gyr (see also Kruijssen et al. 2019a), which roughly coincides with the epoch of transition from the fast to slow accretion regime and the corresponding transition from the rapid rise to steady average star formation rate.

---

[3] The Latte simulations were run using the Gizmo gravity plus hydrodynamics code in mesh-less finite-mass mode (Hopkins 2015) and the FIRE-2 physics model (Hopkins et al. 2018).

[4] http://flathub.flatironinstitute.org/fire

[5] https://wwwmpa.mpa-garching.mpg.de/auriga/gaiamock.html

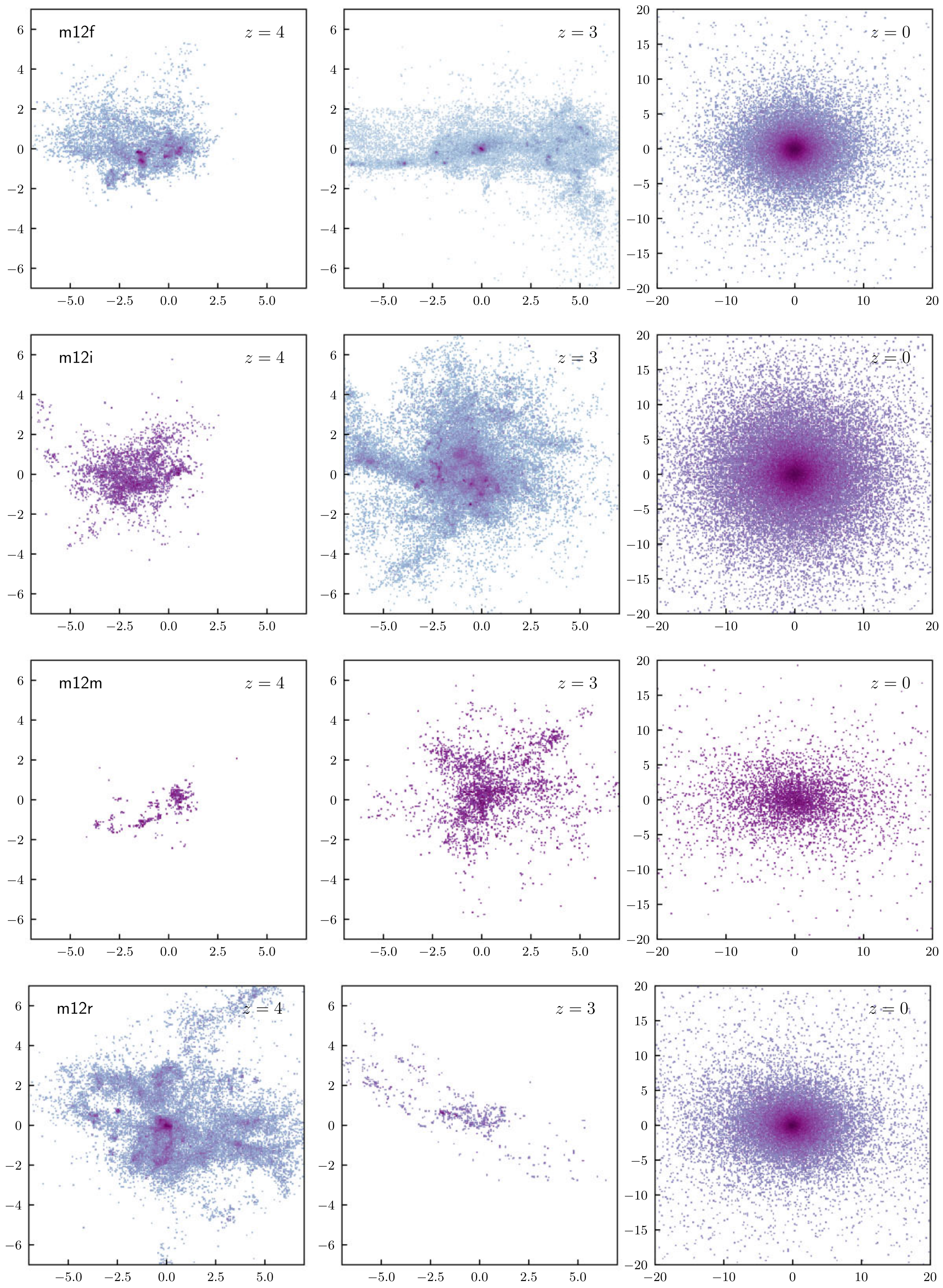

Figure 13. Distribution of stellar particles younger than 100 Myr at $z = 4$ and $z = 3$ (the left two columns in each row) and distribution of the same particles at $z = 0$ (rigtmost panel in each row) projected in the $X - Z$ plane in four representative MW-sized galaxies from the FIRE-2 Latte simulations suite. The coordinates (indicated on the axes) are in physical kpc; note that the range in the left two columns is the same, but is larger in the rightmost column showing $z = 0$ distributions. In each panel the Z axis is aligned with the angular momentum of all stars in the galaxy at the corresponding redshift. The left two columns show a chaotic distribution of young stars forming before the disc formed in each object, while the right-hand column shows that orbital mixing and relaxation result in spheroidal distribution of these stars around galactic centre at the present epoch.

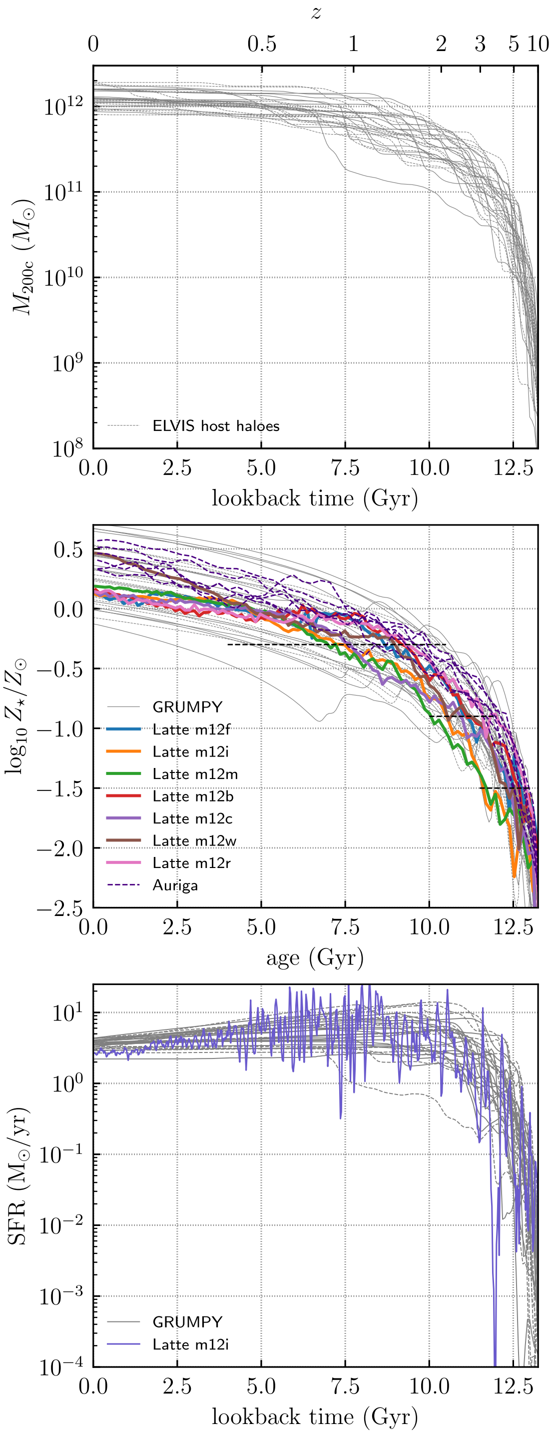

Figure 14. Evolution of halo mass defined within the density contrast 200 times the critical density (top panel), the metallicity–age relation for stars (middle panel), and evolution of star formation rate (bottom panel) for a sample of galaxies forming in Milky Way-sized haloes in the GRUMPY regulator model (Kravtsov & Manwadkar 2021) (thin grey lines), Latte suite of FIRE-2 cosmological zoom-in *N*-body+hydrodynamics simulations of three Milky Way-mass galaxies, `m12f`, `m12i`, and `m12m` (Wetzel et al. 2016) (solid indigo lines). The upper axes in the top panel shows corresponding redshifts. In the middle panel we also show stellar metallicity–age relations in the Auriga simulations of six Milky Way-size haloes (Grand et al. 2018). The three horizontal dashed lines indicate the age range corresponding to the critical metallicities [Fe/H] = −0.3, [Fe/H] = −0.9, [Fe/H] = −1.5 that correspond to metallicity of the Splash, Spin-up, and the lowest metallicity that is probed by the APOGEE data.

The actual distribution of ages of stars in the Latte and Auriga simulations in the metallicity ranges of $[\mathrm{Fe/H}] = -0.3 \pm 0.025$, -0.9 ± 0.025, -1.5 ± 0.025 are shown in Fig. 15. The figure shows that the stars of $[\mathrm{Fe/H}] < -0.9$ are almost all older than 10 Gyr and their distributions have many narrow peaks reflecting strong short-duration bursts of star formation at these early stages of galaxy evolution. The stars of $[\mathrm{Fe/H}] \approx -0.3$ have a considerably broader age distributions centered on ≈6–8 Gyr and with much less prominent peaks, which reflects a considerably less bursty star formation at these later epochs.

The cumulative distributions of stellar mass fraction as a function of age and metallicity are present in Fig. 16, which shows that on average $\lesssim$10 per cent of the final mass is formed in model galaxies in the first 3 Gyr of evolution (i.e. $z \gtrsim 2$), which is consistent with observational constraints for the Milky Way-mass galaxies (e.g. Leitner 2012; van Dokkum et al. 2013). The cumulative distribution as a function of metallicity in the right-hand panel of Fig. 16 is quite similar to the corresponding distribution inferred for the APOGEE data and shown in Fig. 4. In particular, only ≈ 3 per cent of the final stellar mass in the model galaxies form with metallicities $[\mathrm{Fe/H}] < -1$, which is close to the value inferred from the APOGEE data.

4.3 Transition between star formation regimes and formation of the coherently rotating Milky Way disc

The model predictions shown in Fig. 14 indicate that stars with $[\mathrm{Fe/H}] \leq -1$ formed more than 10 Gyr ago (see also Kruijssen et al. 2019a; Agertz et al. 2021). The observed rapid increase in the median V_{tan} at $[\mathrm{Fe/H}] > -1$ thus indicates that a coherent rotating stellar disc formed in the Milky Way progenitor ≈10–11 Gyr ago (or $z \gtrsim 2.5$). This formation epoch is much earlier than the epochs of disc formation for most of the galaxies in the FIRE-2 suite of simulations (Yu et al. 2021; Gurvich et al. 2022; Hafen et al. 2022).

This is also reflected in Fig. 17, which shows the median V_{tan} as a function of age and metallicity for stellar particles in the Milky Way–mass galaxies from the Auriga and Latte simulation suites. Qualitatively, the trends are similar to those of the MW stars shown in Fig. 4: old, low-metallicity stars show little or much smaller mean rotation than younger, higher metallicity stars. Interestingly, at $[\mathrm{Fe/H}] \lesssim -1$ median tangential velocity in both observations and most of the simulated galaxies is small at $V_{\mathrm{tan}} \approx 10$–$60\ \mathrm{km\,s^{-1}}$, but it is not zero. Another similarity is that transition from small to large median V_{tan} occurs over a narrow range of metallicities ($\Delta[\mathrm{Fe/H}] \approx 0.2$–$0.3$). The trend of V_{tan} as a function of stellar age in the left-hand panel shows that this reflects rapid formation of rotating discs over the time period of ≈1–2 Gyr (see also Gurvich et al. 2022). These qualitative similarities lend credence to the interpretation of the observed trend as signalling formation of the Milky Way disc. At the same time, there are interesting differences.

The left-hand panel of the figure shows that transition from small median V_{tan} to value of ≈220–250 $\mathrm{km\,s^{-1}}$ occurs in old stars of ages ≈7–11 Gyr. The exception is the object `m12m`, in which the mean rotation is present with the median $V_{\mathrm{tan}} \approx 100$–$150\ \mathrm{km\,s^{-1}}$ even in the oldest stars, which indicates that there is a significant variation in the timing of such transitions from object to object (see also Yu et al. 2021). Indeed, as can be seen in the results of Santistevan et al. (2020) `m12m` undergoes a significant period of quiescent evolution from $z \approx 5$ to $z \approx 3$, during which its halo mass changed little. Few stars were formed during this period as well. The halo mass then increased tenfold from $z \approx 3$ to $z \approx 2$ and reached the level sufficient to sustain hot halo by the latter epoch leading to formation of a coherently rotating disc where a large fraction of stars formed.

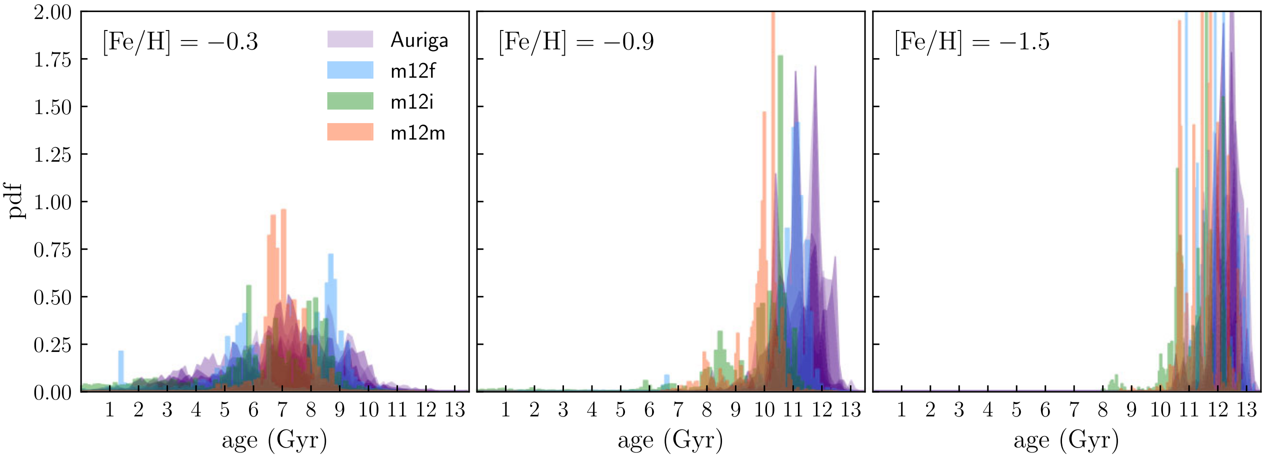

Figure 15. Age distributions of stars with metallicities $[\mathrm{Fe/H}] = -0.3 \pm 0.025,\ -0.9 \pm 0.025,\ -1.5 \pm 0.025$ in the nine simulated MW-mass galaxies from the Latte and Auriga simulations. In both simulation suites stars are selected within $5 < R/\mathrm{kpc} < 11$ and $|Z| < 3$ kpc.

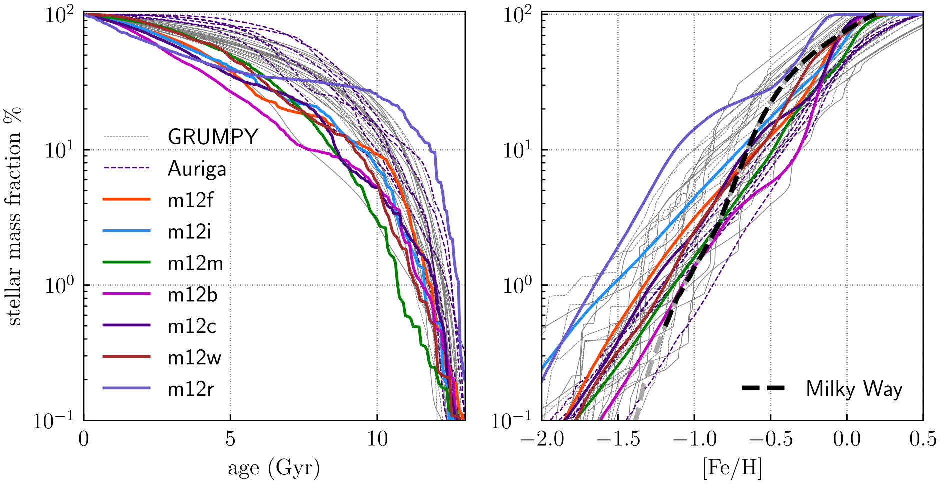

Figure 16. Cumulative stellar mass fraction (in per cent) distribution as a function of stellar age (left-hand panel) and metallicity (right-hand panel). The thin grey lines show results of the GRUMPY model for a suite of Milky Way-sized haloes, while the solid coloured lines show results of the Latte suite of the FIRE-2 simulations. The black/grey dashed line shows the estimate of the *in-situ* stellar mass fraction around the Sun in the Auriga DR17 from the bottom panel of Fig. 4; the grey portion is at metallicities where a certain confusion of the *in-situ* and accreted components exists.

Fig. 18 shows distributions of V_{tan} for stars of different ages and metallicities. In the `m12m` simulation the change of V_{tan} distribution with age is gradual and the form of the V_{tan} distribution of old stars in that simulation is skewed towards positive values, reflecting significant net rotation of old stars in this object. Indeed, even at very low metallicities ([Fe/H]) stars are in a flattened, very thick disc configuration. Evolution of this object is qualitatively consistent with the 'upside-down' scenario of disc formation (Bird et al. 2013, 2021), whereby thick disc is forming first while subsequent generations of stars form in colder gaseous discs forming disc of smaller and smaller scale height. Indeed, as shown in Fig. A1 in the Appendix, old low-metallicity stars in the `m12m` object are distributed in a very thick, albeit somewhat flattened configuration.

However, the distribution as a function of age for the MW-mass object in the `m12f` run in the left-hand panel shows two distinct regimes of evolution: the V_{tan} distribution for stars older than ≈7 Gyr is broad and its mode is close to $0\,\mathrm{km\,s^{-1}}$, while V_{tan} distribution of younger stars is much narrow and is centred on $\approx 250\,\mathrm{km\,s^{-1}}$. The transition between the two forms of distribution is rapid and abrupt for the `m12f` run. The distributions in the two regimes and the rapid transition are also similar in the `m12i`. The 'upside-down' disc formation in these objects occurs during the last ≈6–7 Gyr, while stars forming at earlier times do not form disc at all, but form a nearly spherical distribution (distribution of low-metallicity, old stars in the `m12f` object is shown in Fig. A1).

Formation of the disc in these objects thus does not span their entire evolution history, but is confined to the late stages after the hot inner halo forms. The observations discussed in this study thus probe the transition from the early pre-disc stages evolution of the Milky Way progenitor to formation ('spin-up') of the Milky Way disc that we inhabit and observe today. Isotropic velocity dispersion measured for low-metallicity observed stars indicate that early stages of MW evolution also formed a spheroidal component, while formation of the disc started about 10–11 Gyr ago at $z \approx 2$–3. Obreja et al. (2019) identified a similar spheroidal component in the NIHAO simulations of galaxy formation. They show that this component is kinematically distinct from the bulge, is more spatially extended and is composed almost entirely from the stars formed *in-situ*. Moreover,

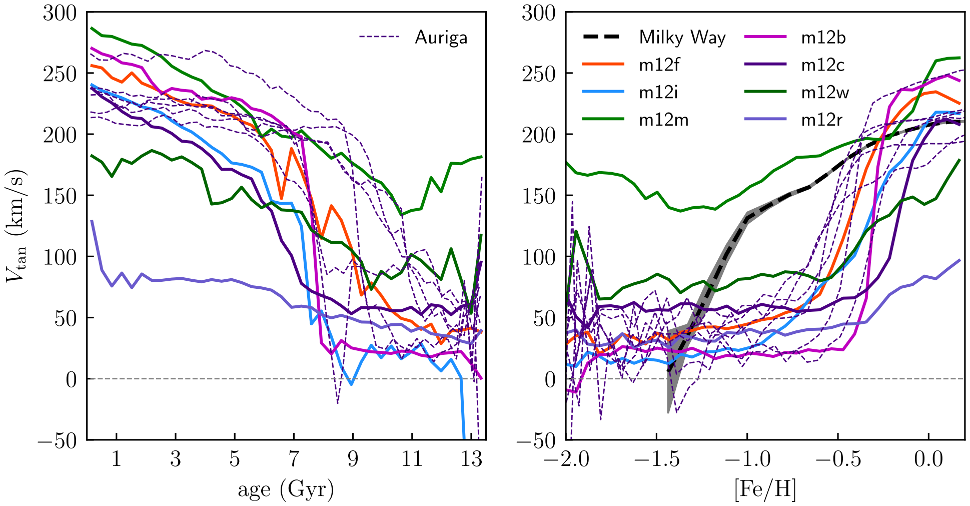

Figure 17. Median tangential velocity of stars in the Latte and Auriga simulations as a function of stellar age (left-hand panel) and metallicity (right-hand panel). The solid coloured lines show median curves for nine simulated Milky Way-sized galaxies, as indicated in the legend. The black dashed line shows the median measurement for the Milky Way obtained using the APOGEE DR17 data with shaded grey area representing 68 per cent uncertainty.

they show that these stars correspond to the earliest episodes of star formation in the Milky Way-sized galaxies. The gas from which these stars form collapses during earliest epochs but loses much of its angular momentum, most likely during collision of gas flowing along different cold streams in the vicinity of the Milky Way progenitor. It therefore forms a spheroidal distribution with little or no net rotation.

The right-hand panels of Fig. 18 show the distribution of $V_{\rm tan}$ for stars of different metallicity and demonstrate that these distribution reveal the two regimes of the star formation similarly to the distributions for age bins, although transition between the two evolution regimes is somewhat smoother due to the scatter between age and metallicity. The overall trend of the distribution shape with stellar metallicity is qualitatively similar to that in the observed stars in the APOGEE survey (see Fig. 5), although the actual shape of the observed low-metallicity stars is not as peaked, while distribution of observed high-metallicity stars is much narrower than in simulations.

One aspect that is similar in both simulations and observations is that the form of the distributions of $V_{\rm tan}$ in the two regime is quite stable and changes only during narrow range of ages or metallicities in the transition between the two regimes. For young, high-metallicity stars this probably simply reflects the fact that they form in the coherent slowly evolving disc. The similarity of the $V_{\rm tan}$ distribution for old, low-metallicity stars probably reflects the common evolutionary and relaxation processes that these stars have experienced. As discussed in Section 4 above, these processes include star formation in extended irregular gas distribution during cold mode gas accretion and dynamical heating and relaxation due to mergers and overall potential fluctuations due to rapid changes in the mass accretion rate and gas removal in feedback-driven winds.

Figs 17 and 18 show that in metallicity transition between the two regimes of evolution is occurring at $[{\rm Fe/H}] \approx -0.8 \div -0.4$ in the simulations, which is considerably larger than in the Milky Way where this transition occurs at $[{\rm Fe/H}] \approx -1.3 \div -1.1$ (see the dashed line). Kinematics of the low-metallicity Milky Way stars thus indicates that the virialization of the inner hot halo and subsequent formation of coherently rotating stellar disc occurred quite early in the evolution of our Galaxy and earlier than in most objects in the FIRE-2 and Auriga suites of simulations. Thus, formation of the hot halo and transition from the fast mass accretion regime with highly bursty star formation to slow accretion regime with steady star formation rate occurred earlier in the Milky Way progenitor.

Current galaxy formation models differ significantly in the amount of short-term burstiness of star formation rate due to different implementations of star formation and feedback (Iyer et al. 2020) with the FIRE-2 simulations exhibiting the strongest short-term burstiness among the models. The measurements presented in this paper indicate that the epoch when star formation in the Milky Way progenitor transitioned from the highly bursty to steady regime approximately coincided with the epoch when the average star formation rate switched from the rapid rise to much slower evolution ≈10–11 Gyr ago. These measurements can thus potentially serve as a useful constraint on the star formation and feedback physics shaping evolution of the Milky Way mass objects during early stages of their evolution.

4.4 Is this scenario consistent with observations of discs in high-z galaxies?

Observations over the past decade revealed existence of stellar and gaseous discs at $z > 3$ (e.g. Stockton et al. 2008; Lelli et al. 2018; Le Fèvre et al. 2020; Neeleman et al. 2020; Rizzo et al. 2020; Tsukui & Iguchi 2021). Although interpretation of the Milky Way observations discussed above implies that disc in the Milky Way-mass galaxies forms only at $z \lesssim 2$–3, it does not actually contradict observations of massive high-z discs. This is because these discs are observed in massive, starbursting galaxies with $M_\star \gtrsim 10^{10}\,M_\odot$ and star formation rates $\gtrsim 200 - 300\,M_\odot\,{\rm yr}^{-1}$. Such large stellar masses and star formation rates at $z \sim 3$–4 indicate that haloes hosting these galaxies have already reached the critical mass threshold required for formation and maintenance of the hot gaseous halo and prevalence of discs in massive high-z galaxies is indeed confirmed by cosmological simulations (Feng et al. 2015; Pillepich et al. 2019). At the same time, the high star formation rates of these galaxies are inconsistent with the typical rates expected for the Milky Way progenitors (e.g. Behroozi et al. 2013, 2019; Moster, Naab & White 2018). These massive discs thus probe formation of the progenitors of modern spheroidal galaxies rather than progenitors of the Milky Way, which have not been directly observable at $z \gtrsim 3$ in the deepest observations so far (e.g. van Dokkum et al. 2013).

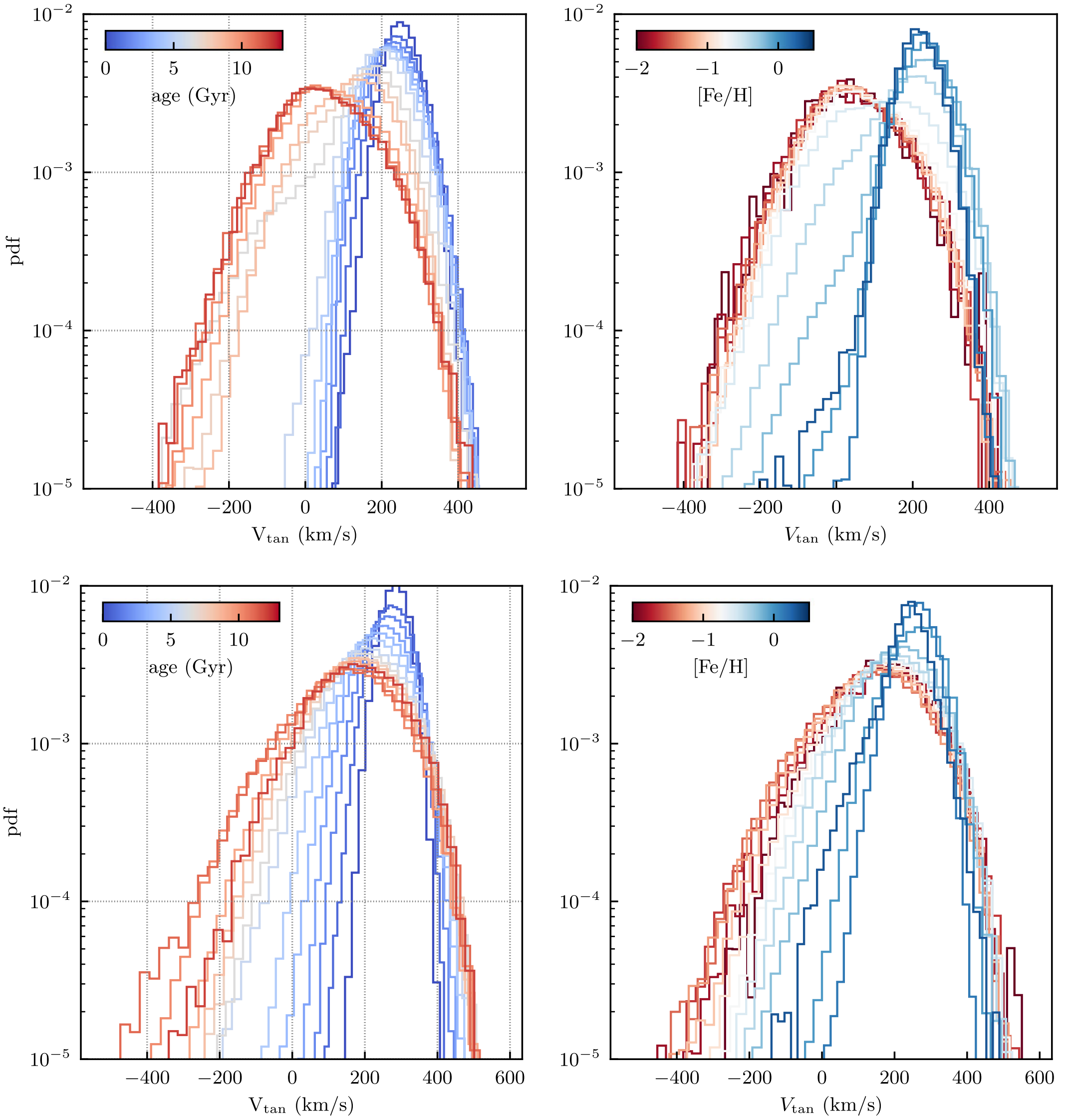

Figure 18. Distributions of the tangential velocity, $V_{\rm tan}$, for stars of different ages (left-hand panels) and metallicities (right-hand panels) for the MW-mass objects in the `m12f` (top row) and `m12m` (bottom row) Latte simulations. The age and metallicity corresponding to each distribution are colour-coded as shown in the colourbar in each panel. The distributions are plotted at constant intervals of age and metallicity, so that rapid transition between old, metal-poor distributions in the upper panels to late, metal-rich coherently rotating distributions correspond to rapid transition from the early pre-disc mode of evolution to formation of coherently rotating disc.

Galaxy formation simulations show that flattened, disc-like configurations can arise at high redshifts during evolution of Milky Way progenitors (e.g. Gnedin & Kravtsov 2010; Tamfal et al. 2022), but such configurations are short-lived at $z > 3$, as gas disc orientation generally changes rapidly and overall gas is often not in a disc configuration at all (Tillson et al. 2015; Meng & Gnedin 2021; Kretschmer et al. 2022).

4.5 Transition between star formation regimes and evolution of scatter in the element ratios

Analyses of the APOGEE DR 17 data presented above showed that the transition from small to large $V_{\rm tan}$ at [Fe/H] $\lesssim -0.9$ is accompanied by a sharp change in scatter in the element abundance ratios [X/Fe] (see Fig. 8). Although detailed interpretation of the variation of scatter for different elements is complicated by the uncertainties in theoretical yields (see e.g. Matteucci 2021, for a recent review) and other modelling aspects (see e.g. Buck et al. 2021) and is beyond the scope of this study, the increase of scatter at low metallicites is generally consistent with the interpretation that low-metallicity stars have formed during the fast gas accretion regime of the Milky Way formation.

It is well known that abundance of a chemical element depends on the gas accretion rate, gas depletion time, and outflow rates (e.g. Peeples & Shankar 2011). During the fast mass accretion stage, all of these factors fluctuate strongly both in time and space, which results in the increase of scatter in metallicity. However, if all elements came from the same source, the scatter in metallicity would not result in scatter of the element ratios as all elements would be distributed similarly. To produce the latter scatter, the enrichment history of different elements must be different which, necessitates contribution of multiple sources to their abundance. Moreover, enrichment by the different sources must be different as a function of time and/or

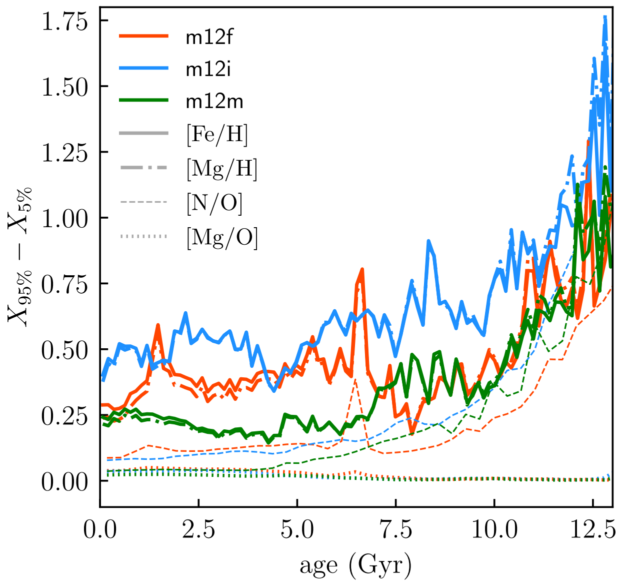

Figure 19. 95 per cent – 5 per cent spread in [Fe/H], [Mg/H], [N/O], and [Mg/O] as a function of age of stellar population in the three galaxies from the Latte suite. Rapid variation in star formation, outflow rate, and depletion time during early stages of evolution (imprinted in the old stars) result in large variations in abundance of all elements (note that the lines for [Fe/H], [Mg/H] are nearly identical). However, the scatter in the element ratios for elements produced by a single source, such as [Mg/O], where both elements are produced exclusively by the core-collapse supernovae, is negligible as both elements vary identically. Scatter in the element ratios, such as [N/O] is, nevertheless, substantial and also sharply increases in old stars, because in this case both SN II and AGB stars contributed significantly to the *N* abundance, but only SN II contribute to O.

metallicity. In this case fluctuations in star formation rate on the time-scales comparable to the enrichment time-scales can result in significant scatter in X/Fe (e.g, Gilmore & Wyse 1991; Johnson & Weinberg 2020).

Moreover, fluctuations in the abundance ratios can also arise even when gas mass is constant, but there are strong temporal and/or spatial variations of gas depletion time (Weinberg, Andrews & Freudenburg 2017; Johnson & Weinberg 2020). The density structure of the highly turbulent interstellar medium during early stages of galaxy evolution should be broad and highly variable. The fraction of dense, star forming gas can thus vary rapidly leading to both spatial and temporal variation of local depletion time. Indeed, Meng et al. (2019) find that local gas depletion times exhibit a wide variation in simulations of high-z progenitors of the MW-sized systems. Large variations in molecular depletion time are also observed in some nearby galaxies with perturbed or unstable gaseous discs and active star formation (e.g. Bolatto et al. 2011; Fisher et al. 2022).

Fig. 19 shows the 95 per cent – 5 per cent in [Fe/H], [Mg/H], [N/O], and [Mg/O] as a function of age of stellar population in the three galaxies from the Latte suite. Rapid variation in star formation, outflow rate, and depletion time during early stages of evolution (imprinted in the old stars) result in large variations in abundance of all elements (note that the lines for [Fe/H], [Mg/H] are nearly identical), while the scatter in the abundance is approximately constant for stars younger than 10 Gyr. However, the scatter in the element ratios for elements produced by a single source, such as [Mg/O], where both elements are produced exclusively by the core-collapse supernovae, is negligible as both elements vary identically. Scatter in the element ratios, such as [N/O] is, nevertheless, substantial and also sharply increases in old stars, because in this case both SN II and AGB stars contributed significantly to the *N* abundance, but only SN II contribute to O.

Similarly, results of the NIHAO simulations of Milky Way-sized galaxies presented by Buck et al. (2021) show that the scatter in element abundance ratios does increase sharply at [Fe/H] $\lesssim -1$ for most enrichment models they considered (see their Figs 9–11). Indicatively, the scatter in this regime is suppressed in the model which assumes that the start of the SN type Ia enrichment is delayed until 158 Myr after the birth of the stellar population. In this case enrichment by SN II and SN Ia occurs at rather different epochs. This implies that the significant scatter is generated when two sources of chemical elements (core-collapse and type Ia SNe in this case) enrich gas at temporally close epochs.

Likewise, in the Latte simulations we see a sharp increase in the spread of [N/Fe] ratio in stars older than ≈10 Gyr or metallicities [Fe/H] $\lesssim -1$, while in other elements tracked in these simulations the increase is gradual. The distinct feature of nitrogen in these simulations, is that both core-collapse supernovae and AGB stars contribute significantly to its abundance on overlapping time-scales, but with rather different time dependence of enrichment by these two sources.

At metallicities [Fe/H] $\lesssim -2$ significant scatter in X/Fe for elements produced by core-collapse supernovae can arise due to strong variations of X/Fe with supernovae progenitor mass (Argast et al. 2000, 2002; Scannapieco, Cescutti & Chiappini 2021). At such small metallicities enrichment of a local ISM patch can be dominated by a single remnant and remnants of different mass exploding at different times after a star formation burst can result in a wide range of X/Fe when subsequent generation of stars forms from the highly inhomogeneously enriched gas.

Galaxy formation models indicate that early stages of galaxy formation, where gas-rich, dense and turbulent environments were prevalent and star formation was bursty, are especially conducive to formation of massive star clusters (e.g. Kravtsov & Gnedin 2005; Kruijssen 2012, 2015; Li et al. 2017; Kim et al. 2018; Pfeffer et al. 2018; Ma et al. 2020). In particular, the fraction of star formation in bound star clusters was shown to be a function of surface density of star formation both in observations (see e.g. Adamo et al. 2020a,b, and references therein) and galaxy formation models (Kruijssen 2012; Li et al. 2017, 2022). Vast majority of massive star clusters that form at high redshifts is expected to dissolve due to high gas mass-loss when gas is removed by stellar winds and supernovae (e.g. Li et al. 2019) and during subsequent evolution due to dynamical heating by strong tides in their natal environment (Fall & Zhang 2001; Li & Gnedin 2019; Li et al. 2022).

These results suggest that a significant fraction of star formation during early stages of the Milky Way formation ($z \gtrsim 2$) occurred in massive star clusters (see e.g. figs 5–8 in Pfeffer et al. 2018). Stars from the massive star clusters formed *in-situ* in the Milky Way progenitor and subsequently dissolved could thus contribute substantially to the *in-situ* population of disc stars. The self-enrichment during cluster formation, which is manifest in observed star clusters (see Section 3.2.3), and associated scatter in element abundances (particularly in C, N, O, Al) will thus be manifest in the disc stars originating from disrupted clusters.

Although the physics of the self-enrichment during cluster formation is not understood (see e.g. section 4 of Bastian & Lardo 2018, for a review of models), we note that there is now a substantial observational evidence that molecular gas in the natal regions of star clusters is cleared by photoionization and stellar feedback within ≲3–5 Myr before the first core-collapse supernovae explode (e.g.

Reggiani et al. 2011; Kos et al. 2019; Kruijssen et al. 2019b; Chevance et al. 2020, 2022; Kim et al. 2021). Such short time frame for star formation in clusters is also strongly indicated by theoretical models (e.g. Li et al. 2017, 2019; Semenov, Kravtsov & Gnedin 2021) and implies that models of cluster enrichment that achieve enrichment of the second generation stars with ≈3–5 Myr (e.g. Prantzos & Charbonnel 2006, see section 4.6 in Bastian & Lardo 2018 for a review) are preferred.

Detailed modelling of the element abundance ratios and their scatter may provide a unique window into the contribution of different sources to the abundances of a given element and associated enrichment time-scales.

5 COMPARISON WITH PREVIOUS WORKS

Aurora, the new *in-situ* spheroidal component revealed in the APOGEE DR17 and *Gaia* EDR3 data in this work has previously eluded identification, primarily due to the lack of detailed elemental abundances that would allow us to differentiate the *in-situ* and the accreted halo stars at low [Fe/H]. Initially, pre-*Gaia* analyses pointed out the existence of a broad-brush dichotomy in the stellar halo's chemokinematic properties (see Chiba & Beers 2000, 2001; Carollo et al. 2007, 2010). According to these authors, the more metal-rich (with typical metallicities around $-1.5 <$ [Fe/H] < -1) and slightly prograde inner stellar halo was distinct from the more metal-poor (with [Fe/H] < -2) and possibly retrograde outer stellar halo (see also Beers et al. 2012; Carollo et al. 2012; An et al. 2013; Santucci et al. 2015).

Gaia astrometry revealed that the strong dependence of the stellar halo kinematics on metallicity was due to the superposition of two accreted components, i.e. the tidal debris from a single massive ancient merger at [Fe/H] ≈ -1.3, i.e. the GS/E material, and contributions from multiple lower-mass accretion events at lower [Fe/H] (see Deason et al. 2018; e.g. Belokurov et al. 2018; Helmi et al. 2018; Mackereth et al. 2019). Note that the first glimpses of the GS/E tidal debris cloud had been seen earlier in Brook et al. (2003), while the dominance of the single massive ancient merger across the inner halo was first established in Deason et al. (2013).

In the last decade, an additional stellar halo component containing stars formed *in-situ* in the Milky Way progenitor was identified using precise elemental abundances (Nissen & Schuster 2010; Hawkins et al. 2015). However, due to relatively small sample sizes used in these studies they probed only metallicities of [Fe/H] $\gtrsim -1$. As discussed in Section 3, most stars in this metallicity range are in a coherently rotating disc and thus have high tangential velocities, but there is a noticeable tail reaching small and retrograde V_{tan}. The latter stars have spheroidal distribution, but were formed in the disc and subsequently dynamically heated during the GS/E merger.

The *Gaia* data was instrumental in confirming the genesis of this *in-situ* halo component, also called the Splash (see e.g. Bonaca et al. 2017; Di Matteo et al. 2019; Gallart et al. 2019; Belokurov et al. 2020). While in the Solar neighbourhood the Splash can contribute as much as a half of all stars on halo-like orbits, it is significantly less extended than the accreted halo (see e.g. Belokurov et al. 2020; Iorio & Belokurov 2021). The chemical properties of the Splash stars are similar (or often indistinguishable) to those of the thick disc (Nissen & Schuster 2010; Fernández-Alvar et al. 2018, 2019; Belokurov et al. 2020; Kordopatis et al. 2020), in agreement with our analysis. Similar to numerical merger simulations, the Milky Way's Splash contains a stellar population on average younger compared to the GS/E debris with a tail of ancient stars (Belokurov et al. 2020; Bonaca et al. 2020) however some disagreement still exists as to the exact star-formation histories of the Splash and the GS/E (c.f. Gallart et al. 2019; Montalbán et al. 2021).

In this study, where the sample size allows us to explore *in-situ* stars with metallicities of [Fe/H] < -1, we showed that these low-metallicity stars constitute a new component, which we called the *Aurora*. These stars have nearly isotropic velocity ellipsoid, little net rotation, and wide distribution of tangential velocities. They also exhibit element abundance ratios distinct from both the accreted halo and the heated disc component. First, the *in-situ* and the accreted stars follow different tracks in [X/Fe] versus [Fe/H] space. Secondly, neither GS/E nor Splash show an excess of the abundance dispersion in Al, Si, N, and O.

Note that *Aurora* stars do not contribute significantly to the Splash population. This is because the heating action of the merging massive satellite is reduced if the velocity dispersion of the host stars is high to begin with and cannot be easily increased much further (see e.g. Grand et al. 2020).

We believe that some of the stars with the largest prograde V_{tan} were previously hypothesized to belong to an ancient metal-weak disc (e.g. Chiba & Beers 2000; Beers et al. 2002; Carollo et al. 2010; Kordopatis et al. 2013; Li & Zhao 2017; Sestito et al. 2019; Di Matteo et al. 2020; Fernández-Alvar et al. 2021). Here, instead of splitting stars into halo and disc, we show that the low-metallicity *in-situ* population has a broad, asymmetric tangential velocity distribution with the mode that is positive but small ($V_{\mathrm{tan}} \approx 50$ km s^{-1}). The tail of the prograde velocities extends to $V_{\mathrm{tan}} \approx 300\,\mathrm{km\,s^{-1}}$, while the tail of retrograde velocities extends to $-200\,\mathrm{km\,s^{-1}}$. The positive mode and the asymmetry create an overabundance of stars with large prograde velocities, but the distribution is continuous and does not show a clear evidence for a distinct disc component. Instead, we argue that the *in-situ* spheroidal component with [Fe/H] < -0.9 is the phase-mixed remnant population of the early turbulent stages of the Milky Way evolution. Note, however, that orbits of some stars that are born in a spheroidal pre-disc component will evolve as the disc grows and as a result the properties of those stars orbiting close to the Galactic plane will appear more discy at the present day (see e.g. Binney & May 1986).

In parallel to the observational studies of the accreted tidal debris, components of stellar halo and their origin were studied using numerical simulations. Nevertheless, to the best of our knowledge the *Aurora* component revealed here has not been previously identified in simulations. A number of studies explored *in-situ* halo (Font et al. 2006, 2011; Zolotov et al. 2009, 2010; Purcell, Bullock & Kazantzidis 2010; McCarthy et al. 2012; Tissera, White & Scannapieco 2012; Tissera et al. 2013, 2014; Cooper et al. 2015; Pillepich, Madau & Mayer 2015), but its main formation mechanism was argued to be dynamical heating and dispersing of the stars born in the inner Galaxy. Often these stars originate (i) inside a (proto)disc and (ii) slightly later compared to the stars in the small-mass dwarfs (e.g. Purcell et al. 2010; Font et al. 2011; McCarthy et al. 2012). Additionally, in many cases, stars formed from the gas accreted from the merging dwarf satellites are attributed to the *in-situ* population (see Tissera et al. 2012; Cooper et al. 2015; Pillepich et al. 2015). Sometimes, stars can form directly out of the hot gaseous halo around the host galaxy, however this mode of *in-situ* star-formation is suspected to be a numerical artefact (see Cooper et al. 2015).

In contrast, as was discussed in detail in the previous section, *Aurora* forms sufficiently early, before any coherent disc is established. Additionally, while the high-redshift prolific accretion activity probably helped us to perturb and displace the low-metallicity stars, we stress that the *Aurora* stars were born in a chaotic state, inherited from the highly turbulent and spatially irregular Galactic ISM at the time.

6 SUMMARY AND CONCLUSIONS

Taking advantage of the exquisite measurements of the element abundances in the APOGEE DR 17 and the *Gaia* EDR3 astrometry, we separate low metallicity stars with $[\mathrm{Fe/H}] \lesssim -0.9$ into the stars born in the Milky Way proper (*in-situ*) and the stars created in low-mass dwarf galaxies and later accreted on to the Milky Way using the [Al/Fe] ratio, as first pointed out by Hawkins et al. (2015). The method exploits the fact that production of aluminium in dwarf galaxies is suppressed and delayed compared to the rapid and prolific enrichment taking place in the early Milky Way. As a result, our low-metallicity *in-situ* sample exhibits negligible contamination by accreted stars and provides the first clear view of the state of our Galaxy's progenitor at high redshifts before and during formation of the disc. Our main results and conclusions are as follows.

(i) We show that the low-metallicity ($[\mathrm{Fe/H}] \lesssim -1.3$) *in-situ* component is kinematically hot with an approximately isotropic velocity ellipsoid and a modest net spin (see Figs 4, 5 and Section 3.1). We use galaxy formation models to establish that stars in this component, which we dub *Aurora*, reflect the chaotic early pre-disc stages of Milky Way's evolution when the first few per cent of its stars form in highly irregular spatial and velocity configurations and which later phase-mix into a spheroidal distribution (Section 4.1 and Fig. 13).

(ii) We demonstrate that the low-metallicity stars of the *Aurora* component exhibit a large scatter in element abundances (Section 3.2 and e.g. Figs 7, 11). By comparing tracks of individual elements referenced to either Fe or Mg we show that in the early Milky Way, across a variety of chemical elements, the observed scatter of the element ratios is likely caused by the increased stochasticity in metallicity at early times driven by strong variations in gas accretion and gas outflow rates and associated burstiness of star formation (Section 4.5).

(iii) In addition, Al, Si, N, and O ratios to either Fe or Mg display an even larger scatter at low metallicities. Comparisons with the anomalous chemical patterns observed in the Milky Way globular clusters indicates that nucleosynthetic channels acting inside massive stellar agglomerations may have contributed significantly to the overall enrichment of the early Milky Way (Section 3.2.3, Fig. 12).

(iv) The median tangential velocity of the *in-situ* stars increases sharply with increasing metallicity between $[\mathrm{Fe/H}] = -1.3$ and -0.9 (Section 3.1 and Fig. 4). The observed and theoretically expected age-metallicity correlations imply that this increase reflects a rapid formation of the Milky Way disc over ≈1–2 Gyr, during which it spins up and settles into a coherently rotating, thick disc with a median azimuthal velocity of $V_{\mathrm{tan}} \approx 150\ \mathrm{km\ s^{-1}}$ at $[\mathrm{Fe/H}] \approx -0.9$.

(v) Observations and theoretical models indicate that violent head-on collision with the GS/E dwarf galaxy, which dramatically transformed some of the disc stellar orbits, as manifested in the Splash stellar component, has occurred after formation of the thick disc in the MW's progenitor.

In galaxy formation models gas distribution in the central regions of young Milky Way analogues is highly irregular, turbulent, and rapidly evolving due to a combined effects of supersonic cold filamentary flows and feedback-driven winds. Stars born in the densest regions of this gas inherit its irregular distribution and stellar component of most progenitors of the MW-sized galaxies thus does not develop a persistent rotating disc during these epochs. Recent analyses of galaxy formation simulations showed that formation of the disc starts when galaxy is able to build up and sustain hot gaseous halo, which changes the mode of gas accretion and allows development of coherently rotating disc. The thick disc likely forms during this transition, while the subsequent evolution when gas is accreted via a steady cooling flow leads to a stable disc orientation and build-up of the thin disc.

Most importantly, we stress that the absolute majority, i.e. 12 out of 13 of the numerical simulations studied here exhibit qualitatively similar chemokinematic behaviour observed in the Milky Way. Specifically, at the metallicities corresponding to the look-back times between 8 and 12 Gyr, most model Milky Way analogues have low-amplitude net spin but no coherent disc. The spin-up transition uncovered in this work is a ubiquitous feature in these models with the young Milky Ways in both Auriga and FIRE simulations undergoing a fast transition from a messy slowly rotating *Aurora*-like stellar component to a fast rotating disc.

Interestingly, in most of these models the spin-up transition happens at significantly larger metallicities than observed in the Milky Way. If we assume that the spin-up observed in the Milky Way is typical, there may be several possible reasons for this difference. First, note that the low-metallicity *in-situ* stars probing this transition constitute only a few per cent of the final stellar mass (see Figs 4 and 16). To reproduce the observed spin-up metallicity simulations must correctly model both the early star formation history and chemical enrichment of this component (including removal of heavy elements by winds) and thermodynamical processes related to the formation of hot gaseous halo and related dynamical processes leading to disc formation. Given these considerations, discrepancy with current generation of simulations is not surprising. At the same time, going forward the observed spin-up will provide a sensitive probe of the physics of these processes and their treatment in galaxy formation simulations.

We use galaxy formation simulations and results of chemical enrichment models to show that the elevated scatter in stellar metallicity and abundance ratios is driven by strong bursts of star formation during early pre-disc stages of evolution (see Section 4.5). The bursts are often separated by gaps in star formation activity. The corresponding gaseous outflows and ongoing fresh gas accretion result in large scatter in element abundances. In particular, we show that low-metallicity stars born in the FIRE-2 suite of simulations clearly display rapid increase of metallicity dispersion with decreasing metallicity for stars born during the pre-disc phase.

Additionally, we use simulations to explicitly show that scatter in chemical abundance ratios can be pushed up when multiple stellar sources contribute to abundance of a given chemical element on different time-scales, while scatter in the abundance ratios are negligible if the two elements in the ratio are produced by the same single source. While multiple sources are thought to contribute to the abundance of most chemical species, details of these processes are uncertain and their modelling in the current simulations of galaxy formation and chemical enrichment is not yet adequate for a direct detailed comparisons with observations trends.

Results of this study indicate that the low metallicity tail of Milky Way's stellar population provides a unique window into the tumultuous state of the Galaxy in its pre-disc and disc formation stages. This may be our only view of the detailed evolution of Milky Way-sized galaxies as their expected stellar masses and star formation rates are too low to be directly observable at $z \gtrsim 2$. Future spectroscopic surveys such as DESI, WEAVE, 4MOST, and SDSS V will significantly increase the size of the low-metallicity sample and this should provide multiple exciting avenues for exploration.

ACKNOWLEDGEMENTS

The authors are grateful to Keith Hawkins, Kathryn Johnston, Thomas Masseron, Julianne Dalcanton, David Hogg, Adrian Price-Whelan, Zephyr Penoyre, David Aguado, Daniel Anglés-Alcázar, Drummond Fielding, Wyn Evans, Andreea Font, Freeke van de Voort, and the members of the Cambridge Streams and UChicago Friday Owls Clubs for many enlightening conversations that helped us to improve the quality of this work. We are also grateful to Claude-André Faucher-Giguere and Jonathan Stern for comments and sharing their paper (Gurvich et al. 2022) ahead of publication. Many thanks to the anonymous referee for the thorough reading of the manuscript and their helpful comments. AK would also like to thank Institute of Astronomy at Cambridge University and its Sackler visitor program for the warm hospitality during his 2018-2019 visit. His work on this project was supported by the National Science Foundation grants AST-1714658 and AST-1911111 and NASA ATP grant 80NSSC20K0512.

In this study, we have used the Ananke data base of the Latte simulations (http://fire.northwestern.edu/ananke/), FIRE-2 simulation public data (http://flathub.flatironinstitute.org/fire), and Auriga (http://wwwmpa.mpa-garching.mpg.de/auriga/) simulation teams for making their simulation results publicly available. We use simulations from the FIRE-2 public data release (Wetzel et al. 2022). The FIRE-2 cosmological zoom-in simulations of galaxy formation are part of the Feedback In Realistic Environments (FIRE) project, generated using the Gizmo code (Hopkins 2015) and the FIRE-2 physics model (Hopkins et al. 2018).

This research made use of data from the European Space Agency mission *Gaia* (http://www.cosmos.esa.int/gaia), processed by the *Gaia* Data Processing and Analysis Consortium (DPAC, http://www.cosmos.esa.int/web/gaia/dpac/consortium). Funding for the DPAC has been provided by national institutions, in particular the institutions participating in the *Gaia* Multilateral Agreement. This paper made used of the Whole Sky Data base (wsdb) created by Sergey Koposov and maintained at the Institute of Astronomy, Cambridge with financial support from the Science and Technology Facilities Council (STFC) and the European Research Council (ERC).

DATA AVAILABILITY

This study uses `allStarLite-dr17-synspec_rev1` and `apogee_astroNN-DR17` catalogues publicly available at https://www.sdss.org/dr17/irspec/spectro_data/.

REFERENCES

Abadi M. G., Navarro J. F., Steinmetz M., Eke V. R., 2003, ApJ, 591, 499
Abdurro'uf et al., 2022, ApJS, 259, 35
Adamo A. et al., 2020a, Space Sci. Rev., 216, 69
Adamo A. et al., 2020b, MNRAS, 499, 3267
Agertz O., Kravtsov A. V., Leitner S. N., Gnedin N. Y., 2013, ApJ, 770, 25
Agertz O. et al., 2021, MNRAS, 503, 5826
Alencastro Puls A., Casagrande L., Monty S., Yong D., Liu F., Stello D., Aguirre Børsen-Koch V., Freeman K. C., 2022, MNRAS, 510, 1733
Amarante J. A. S., Smith M. C., Boeche C., 2020, MNRAS, 492, 3816
An D. et al., 2013, ApJ, 763, 65
Argast D., Samland M., Gerhard O. E., Thielemann F. K., 2000, A&A, 356, 873
Argast D., Samland M., Thielemann F. K., Gerhard O. E., 2002, A&A, 388, 842
Bastian N., Lardo C., 2018, ARA&A, 56, 83
Beers T. C., Drilling J. S., Rossi S., Chiba M., Rhee J., Führmeister B., Norris J. E., von Hippel T., 2002, AJ, 124, 931
Beers T. C. et al., 2012, ApJ, 746, 34
Behroozi P. S., Wechsler R. H., Conroy C., 2013, ApJ, 770, 57
Behroozi P., Wechsler R. H., Hearin A. P., Conroy C., 2019, MNRAS, 488, 3143
Belokurov V., Erkal D., Evans N. W., Koposov S. E., Deason A. J., 2018, MNRAS, 478, 611
Belokurov V., Sanders J. L., Fattahi A., Smith M. C., Deason A. J., Evans N. W., Grand R. J. J., 2020, MNRAS, 494, 3880
Binney J., 2013, New Astron. Rev., 57, 29
Binney J., May A., 1986, MNRAS, 218, 743
Bird J. C., Kazantzidis S., Weinberg D. H., Guedes J., Callegari S., Mayer L., Madau P., 2013, ApJ, 773, 43
Bird J. C., Loebman S. R., Weinberg D. H., Brooks A. M., Quinn T. R., Christensen C. R., 2021, MNRAS, 503, 1815
Birnboim Y., Dekel A., 2003, MNRAS, 345, 349
Bolatto A. D. et al., 2011, ApJ, 741, 12
Bonaca A., Conroy C., Wetzel A., Hopkins P. F., Kereš D., 2017, ApJ, 845, 101
Bonaca A. et al., 2020, ApJ, 897, L18
Bovy J., 2015, ApJS, 216, 29
Brook C. B., Kawata D., Gibson B. K., Flynn C., 2003, ApJ, 585, L125
Brook C. B., Kawata D., Gibson B. K., Freeman K. C., 2004, ApJ, 612, 894
Buck T., Rybizki J., Buder S., Obreja A., Macciò A. V., Pfrommer C., Steinmetz M., Ness M., 2021, MNRAS, 508, 3365
Burkert A., Truran J. W., Hensler G., 1992, ApJ, 391, 651
Carollo D. et al., 2007, Nature, 450, 1020
Carollo D. et al., 2010, ApJ, 712, 692
Carollo D. et al., 2012, ApJ, 744, 195
Carretta E., Bragaglia A., Gratton R., Lucatello S., 2009, A&A, 505, 139
Carretta E., Bragaglia A., Gratton R. G., Recio-Blanco A., Lucatello S., D'Orazi V., Cassisi S., 2010, A&A, 516, A55
Cayrel R. et al., 2004, A&A, 416, 1117
Chevance M. et al., 2020, MNRAS, 493, 2872
Chevance M. et al., 2022, MNRAS, 509, 272
Chiba M., Beers T. C., 2000, AJ, 119, 2843
Chiba M., Beers T. C., 2001, ApJ, 549, 325
Cooper A. P., Parry O. H., Lowing B., Cole S., Frenk C., 2015, MNRAS, 454, 3185
Cottrell P. L., Da Costa G. S., 1981, ApJ, 245, L79
Crain R. A. et al., 2015, MNRAS, 450, 1937
Danovich M., Dekel A., Hahn O., Ceverino D., Primack J., 2015, MNRAS, 449, 2087
Das P., Hawkins K., Jofré P., 2020, MNRAS, 493, 5195
Deason A. J., Belokurov V., Evans N. W., Johnston K. V., 2013, ApJ, 763, 113
Deason A. J., Belokurov V., Koposov S. E., Lancaster L., 2018, ApJ, 862, L1
Dekel A., Birnboim Y., 2006, MNRAS, 368, 2
Dekel A. et al., 2009, Nature, 457, 451
Dekel A., Ginzburg O., Jiang F., Freundlich J., Lapiner S., Ceverino D., Primack J., 2020, MNRAS, 493, 4126
Denissenkov P. A., Hartwick F. D. A., 2014, MNRAS, 437, L21
Di Matteo P., Haywood M., Lehnert M. D., Katz D., Khoperskov S., Snaith O. N., Gómez A., Robichon N., 2019, A&A, 632, A4
Di Matteo P., Spite M., Haywood M., Bonifacio P., Gómez A., Spite F., Caffau E., 2020, A&A, 636, A115
Dillamore A. M., Belokurov V., Font A. S., McCarthy I. G., 2022, MNRAS, 513, 1867
Eggen O. J., Lynden-Bell D., Sandage A. R., 1962, ApJ, 136, 748
Fall S. M., Zhang Q., 2001, ApJ, 561, 751
Feng Y., Di Matteo T., Croft R., Tenneti A., Bird S., Battaglia N., Wilkins S., 2015, ApJ, 808, L17
Fernández-Alvar E. et al., 2018, ApJ, 852, 50
Fernández-Alvar E., Tissera P. B., Carigi L., Schuster W. J., Beers T. C., Belokurov V. A., 2019, MNRAS, 485, 1745
Fernández-Alvar E. et al., 2021, MNRAS, 508, 1509

Fernández-Trincado J. G., Beers T. C., Minniti D., Tang B., Villanova S., Geisler D., Pérez-Villegas A., Vieira K., 2020, A&A, 643, L4

Feuillet D. K., Bovy J., Holtzman J., Girardi L., MacDonald N., Majewski S. R., Nidever D. L., 2016, ApJ, 817, 40

Feuillet D. K., Frankel N., Lind K., Frinchaboy P. M., García-Hernández D. A., Lane R. R., Nitschelm C., Roman-Lopes A., 2019, MNRAS, 489, 1742

Fisher D. B., Bolatto A. D., Glazebrook K., Obreschkow D., Abraham R. G., Kacprzak G. G., Nielsen N. M., 2022, ApJ, 928, 169

Flores Velázquez J. A. et al., 2021, MNRAS, 501, 4812

Font A. S., Navarro J. F., Stadel J., Quinn T., 2001, ApJ, 563, L1

Font A. S., Johnston K. V., Bullock J. S., Robertson B. E., 2006, ApJ, 646, 886

Font A. S., McCarthy I. G., Crain R. A., Theuns T., Schaye J., Wiersma R. P. C., Dalla Vecchia C., 2011, MNRAS, 416, 2802

Freeman K., Bland-Hawthorn J., 2002, ARA&A, 40, 487

Gaia Collaboration 2016, A&A, 595, A1

Gallart C., Bernard E. J., Brook C. B., Ruiz-Lara T., Cassisi S., Hill V., Monelli M., 2019, Nat. Astron., 3, 932

Garrison-Kimmel S., Boylan-Kolchin M., Bullock J. S., Lee K., 2014, MNRAS, 438, 2578

Gilmore G., Reid N., 1983, MNRAS, 202, 1025

Gilmore G., Wyse R. F. G., 1991, ApJ, 367, L55

Gnedin N. Y., Kravtsov A. V., 2010, ApJ, 714, 287

Grand R. J. J. et al., 2018, MNRAS, 481, 1726

Grand R. J. J. et al., 2020, MNRAS, 497, 1603

Gratton R., Sneden C., Carretta E., 2004, ARA&A, 42, 385

Grunblatt S. K. et al., 2021, ApJ, 916, 88

Guedes J., Callegari S., Madau P., Mayer L., 2011, ApJ, 742, 76

Gurvich A. B. et al., 2022, MNRAS, (arXiv:2203.04321)

Hafen Z. et al., 2022, preprint (arXiv:2201.07235)

Hasselquist S. et al., 2021, ApJ, 923, 172

Hawkins K., Jofré P., Masseron T., Gilmore G., 2015, MNRAS, 453, 758

Hayashi H., Chiba M., 2006, PASJ, 58, 835

Hayes C. R. et al., 2018, ApJ, 852, 49

Haywood M., Di Matteo P., Lehnert M. D., Katz D., Gómez A., 2013, A&A, 560, A109

Haywood M., Di Matteo P., Lehnert M. D., Snaith O., Khoperskov S., Gómez A., 2018, ApJ, 863, 113

Helmi A., Babusiaux C., Koppelman H. H., Massari D., Veljanoski J., Brown A. G. A., 2018, Nature, 563, 85

Hidalgo S. L. et al., 2011, ApJ, 730, 14

Hopkins P. F., 2015, MNRAS, 450, 53

Hopkins P. F., Quataert E., Murray N., 2011, MNRAS, 417, 950

Hopkins P. F., Quataert E., Murray N., 2012, MNRAS, 421, 3522

Hopkins P. F. et al., 2018, MNRAS, 480, 800

Horta D. et al., 2021, MNRAS, 500, 1385

Iorio G., Belokurov V., 2019, MNRAS, 482, 3868

Iorio G., Belokurov V., 2021, MNRAS, 502, 5686

Iyer K. G. et al., 2020, MNRAS, 498, 430

Johnson J. W., Weinberg D. H., 2020, MNRAS, 498, 1364

Jones B. J. T., Wyse R. F. G., 1983, A&A, 120, 165

Katz D., Gómez A., Haywood M., Snaith O., Di Matteo P., 2021, A&A, 655, A111

Kazantzidis S., Bullock J. S., Zentner A. R., Kravtsov A. V., Moustakas L. A., 2008, ApJ, 688, 254

Kazantzidis S., Zentner A. R., Kravtsov A. V., Bullock J. S., Debattista V. P., 2009, ApJ, 700, 1896

Kereš D., Katz N., Weinberg D. H., Davé R., 2005, MNRAS, 363, 2

Kereš D., Katz N., Fardal M., Davé R., Weinberg D. H., 2009, MNRAS, 395, 160

Kim J.-h. et al., 2018, MNRAS, 474, 4232

Kim J. et al., 2021, MNRAS, 504, 487

Koch A., Grebel E. K., Martell S. L., 2019, A&A, 625, A75

Koppelman H., Helmi A., Veljanoski J., 2018, ApJ, 860, L11

Koppelman H. H., Helmi A., Massari D., Price-Whelan A. M., Starkenburg T. K., 2019, A&A, 631, L9

Kordopatis G. et al., 2013, MNRAS, 436, 3231

Kordopatis G., Recio-Blanco A., Schultheis M., Hill V., 2020, A&A, 643, A69

Kos J. et al., 2019, A&A, 631, A166

Kravtsov A. V., Gnedin O. Y., 2005, ApJ, 623, 650

Kravtsov A., Manwadkar V., 2021, MNRAS, preprint (arXiv:2106.09724)

Kretschmer M., Dekel A., Teyssier R., 2022, MNRAS, 510, 3266

Kruijssen J. M. D., 2012, MNRAS, 426, 3008

Kruijssen J. M. D., 2015, MNRAS, 454, 1658

Kruijssen J. M. D., Pfeffer J. L., Reina-Campos M., Crain R. A., Bastian N., 2019a, MNRAS, 486, 3180

Kruijssen J. M. D. et al., 2019b, Nature, 569, 519

Lane J. M. M., Bovy J., Mackereth J. T., 2022, MNRAS, 510, 5119

Le Fèvre O. et al., 2020, A&A, 643, A1

Leitner S. N., 2012, ApJ, 745, 149

Lelli F., De Breuck C., Falkendal T., Fraternali F., Man A. W. S., Nesvadba N. P. H., Lehnert M. D., 2018, MNRAS, 479, 5440

Leung H. W., Bovy J., 2019, MNRAS, 489, 2079

Li H., Gnedin O. Y., 2019, MNRAS, 486, 4030

Li C., Zhao G., 2017, ApJ, 850, 25

Li H., Gnedin O. Y., Gnedin N. Y., Meng X., Semenov V. A., Kravtsov A. V., 2017, ApJ, 834, 69

Li H., Vogelsberger M., Marinacci F., Gnedin O. Y., 2019, MNRAS, 487, 364

Li H., Vogelsberger M., Bryan G. L., Marinacci F., Sales L. V., Torrey P., 2022, MNRAS, in press

Lind K. et al., 2015, A&A, 575, L12

Ma X., Hopkins P. F., Wetzel A. R., Kirby E. N., Anglés-Alcázar D., Faucher-Giguère C.-A., Kereš D., Quataert E., 2017, MNRAS, 467, 2430

Ma X. et al., 2020, MNRAS, 493, 4315

Mackereth J. T., Bovy J., 2018, PASP, 130, 114501

Mackereth J. T. et al., 2019, MNRAS, 482, 3426

McCarthy I. G., Font A. S., Crain R. A., Deason A. J., Schaye J., Theuns T., 2012, MNRAS, 420, 2245

Malhan K. et al., 2022, ApJ, 926, 107

Mandelker N., Nagai D., Aung H., Dekel A., Padnos D., Birnboim Y., 2019, MNRAS, 484, 1100

Mandelker N., Nagai D., Aung H., Dekel A., Birnboim Y., van den Bosch F. C., 2020, MNRAS, 494, 2641

Mandelker N., van den Bosch F. C., Springel V., van de Voort F., Burchett J. N., Butsky I. S., Nagai D., Oh S. P., 2021, ApJ, 923, 115

Martell S. L., Smolinski J. P., Beers T. C., Grebel E. K., 2011, A&A, 534, A136

Martell S. L. et al., 2016, ApJ, 825, 146

Masseron T. et al., 2019, A&A, 622, A191

Matteucci F., 2021, A&AR, 29, 5

Meng X., Gnedin O. Y., 2021, MNRAS, 502, 1433

Meng X., Gnedin O. Y., Li H., 2019, MNRAS, 486, 1574

Montalbán J. et al., 2021, Nat. Astron., 5, 640

Morrison H. L., Flynn C., Freeman K. C., 1990, AJ, 100, 1191

Moster B. P., Naab T., White S. D. M., 2018, MNRAS, 477, 1822

Myeong G. C., Evans N. W., Belokurov V., Amorisco N. C., Koposov S. E., 2018a, MNRAS, 475, 1537

Myeong G. C., Evans N. W., Belokurov V., Sanders J. L., Koposov S. E., 2018b, MNRAS, 478, 5449

Myeong G. C., Evans N. W., Belokurov V., Sanders J. L., Koposov S. E., 2018c, ApJ, 856, L26

Naab T., Ostriker J. P., 2017, ARA&A, 55, 59

Naidu R. P., Conroy C., Bonaca A., Johnson B. D., Ting Y.-S., Caldwell N., Zaritsky D., Cargile P. A., 2020, ApJ, 901, 48

Neeleman M., Prochaska J. X., Kanekar N., Rafelski M., 2020, Nature, 581, 269

Nissen P. E., Schuster W. J., 2010, A&A, 511, L10

Nomoto K., Kobayashi C., Tominaga N., 2013, ARA&A, 51, 457

Norris J., Bessell M. S., Pickles A. J., 1985, ApJS, 58, 463

Obreja A., Domínguez-Tenreiro R., Brook C., Martínez-Serrano F. J., Doménech-Moral M., Serna A., Mollá M., Stinson G., 2013, ApJ, 763, 26

Obreja A. et al., 2019, MNRAS, 487, 4424

Pancino E. et al., 2017, A&A, 601, A112

Peeples M. S., Shankar F., 2011, MNRAS, 417, 2962

Pfeffer J., Kruijssen J. M. D., Crain R. A., Bastian N., 2018, MNRAS, 475, 4309

Pichon C., Pogosyan D., Kimm T., Slyz A., Devriendt J., Dubois Y., 2011, MNRAS, 418, 2493

Pillepich A., Madau P., Mayer L., 2015, ApJ, 799, 184

Pillepich A. et al., 2019, MNRAS, 490, 3196

Prantzos N., Charbonnel C., 2006, A&A, 458, 135

Prantzos N., Charbonnel C., Iliadis C., 2007, A&A, 470, 179

Prantzos N., Charbonnel C., Iliadis C., 2017, A&A, 608, A28

Purcell C. W., Bullock J. S., Kazantzidis S., 2010, MNRAS, 404, 1711

Quinn P. J., Hernquist L., Fullagar D. P., 1993, ApJ, 403, 74

Reggiani M., Robberto M., Da Rio N., Meyer M. R., Soderblom D. R., Ricci L., 2011, A&A, 534, A83

Renzini A. et al., 2015, MNRAS, 454, 4197

Rizzo F., Vegetti S., Powell D., Fraternali F., McKean J. P., Stacey H. R., White S. D. M., 2020, Nature, 584, 201

Rosdahl J., Blaizot J., 2012, MNRAS, 423, 344

Ryan S. G., Lambert D. L., 1995, AJ, 109, 2068

Sales L. V., Navarro J. F., Theuns T., Schaye J., White S. D. M., Frenk C. S., Crain R. A., Dalla Vecchia C., 2012, MNRAS, 423, 1544

Sanders J. L., Das P., 2018, MNRAS, 481, 4093

Santistevan I. B., Wetzel A., El-Badry K., Bland-Hawthorn J., Boylan-Kolchin M., Bailin J., Faucher-Giguère C.-A., Benincasa S., 2020, MNRAS, 497, 747

Santucci R. M. et al., 2015, ApJ, 813, L16

Scannapieco C., Cescutti G., Chiappini C., 2021, preprint (arXiv:2107.05653)

Schiavon R. P. et al., 2017, MNRAS, 465, 501

Semenov V. A., Kravtsov A. V., Gnedin N. Y., 2021, ApJ, 918, 13

Sestito F. et al., 2019, MNRAS, 484, 2166

Silva Aguirre V. et al., 2018, MNRAS, 475, 5487

Stern J. et al., 2021, ApJ, 911, 88

Stewart K. R., Kaufmann T., Bullock J. S., Barton E. J., Maller A. H., Diemand J., Wadsley J., 2011, ApJ, 738, 39

Stewart K. R., Brooks A. M., Bullock J. S., Maller A. H., Diemand J., Wadsley J., Moustakas L. A., 2013, ApJ, 769, 74

Stewart K. R. et al., 2017, ApJ, 843, 47

Stinson G. S., Brook C., Macciò A. V., Wadsley J., Quinn T. R., Couchman H. M. P., 2013, MNRAS, 428, 129

Stockton A., McGrath E., Canalizo G., Iye M., Maihara T., 2008, ApJ, 672, 146

Tamfal T., Mayer L., Quinn T. R., Babul A., Madau P., Capelo P. R., Shen S., Staub M., 2022, ApJ, 928, 106

Tillson H., Devriendt J., Slyz A., Miller L., Pichon C., 2015, MNRAS, 449, 4363

Tissera P. B., White S. D. M., Scannapieco C., 2012, MNRAS, 420, 255

Tissera P. B., Scannapieco C., Beers T. C., Carollo D., 2013, MNRAS, 432, 3391

Tissera P. B., Beers T. C., Carollo D., Scannapieco C., 2014, MNRAS, 439, 3128

Tsukui T., Iguchi S., 2021, Science, 372, 1201

Twarog B. A., Anthony-Twarog B. J., 1994, AJ, 107, 1371

van Dokkum P. G. et al., 2013, ApJ, 771, L35

Vasiliev E., Belokurov V., Evans W., 2022, ApJ, 926 , 203

Velazquez H., White S. D. M., 1999, MNRAS, 304, 254

Villalobos Á., Helmi A., 2008, MNRAS, 391, 1806

Vogelsberger M., Genel S., Sijacki D., Torrey P., Springel V., Hernquist L., 2013, MNRAS, 436, 3031

Weinberg D. H., Andrews B. H., Freudenburg J., 2017, ApJ, 837, 183

Weinberg D. H. et al., 2019, ApJ, 874, 102

Wetzel A. R., Hopkins P. F., Kim J.-h., Faucher-Giguère C.-A., Kereš D., Quataert E., 2016, ApJ, 827, L23

Wetzel A. et al., 2022, preprint (arXiv:2202.06969)

Wheeler J. C., Sneden C., Truran James W. J., 1989, ARA&A, 27, 279

Woosley S. E., Weaver T. A., 1995, ApJS, 101, 181

Yong D., Grundahl F., Nissen P. E., Jensen H. R., Lambert D. L., 2005, A&A, 438, 875

Yu S. et al., 2021, MNRAS, 505, 889

Yuan Z. et al., 2020, ApJ, 891, 39

Zolotov A., Willman B., Brooks A. M., Governato F., Brook C. B., Hogg D. W., Quinn T., Stinson G., 2009, ApJ, 702, 1058

Zolotov A., Willman B., Brooks A. M., Governato F., Hogg D. W., Shen S., Wadsley J., 2010, ApJ, 721, 738

APPENDIX A: DISTRIBUTION OF STARS IN THE FIRE SIMULATIONS

Fig. A1 shows distribution of the *in-situ* stellar particles at $z = 0$ of two MW-sized galaxies from the FIRE suite (`m12f` and `m12m`) in the $Z - R$ plane, where Z is the distance from the plane of the disc defined as the plane perpendicular to the angular momentum of all stars and R is the galactocentric distance. The figure shows stars with $-0.2 < \mathrm{[Fe/H]} < 0.5$ (left-hand panels) that form in the last several Gyrs and are distributed in a discy configuration and metal poor stars with $-1.5 < \mathrm{[Fe/H]} < -1$ (right-hand panels) that form during earlier chaotic epochs. The figure shows that low-metallicity stars have a spheroidal distribution at the shown $z = 0$ epoch, even in `m12m`, in which stars forming at $z > 2$ exhibited coherent rotation (although they did not form in a well-defined disc, see Fig. 13).

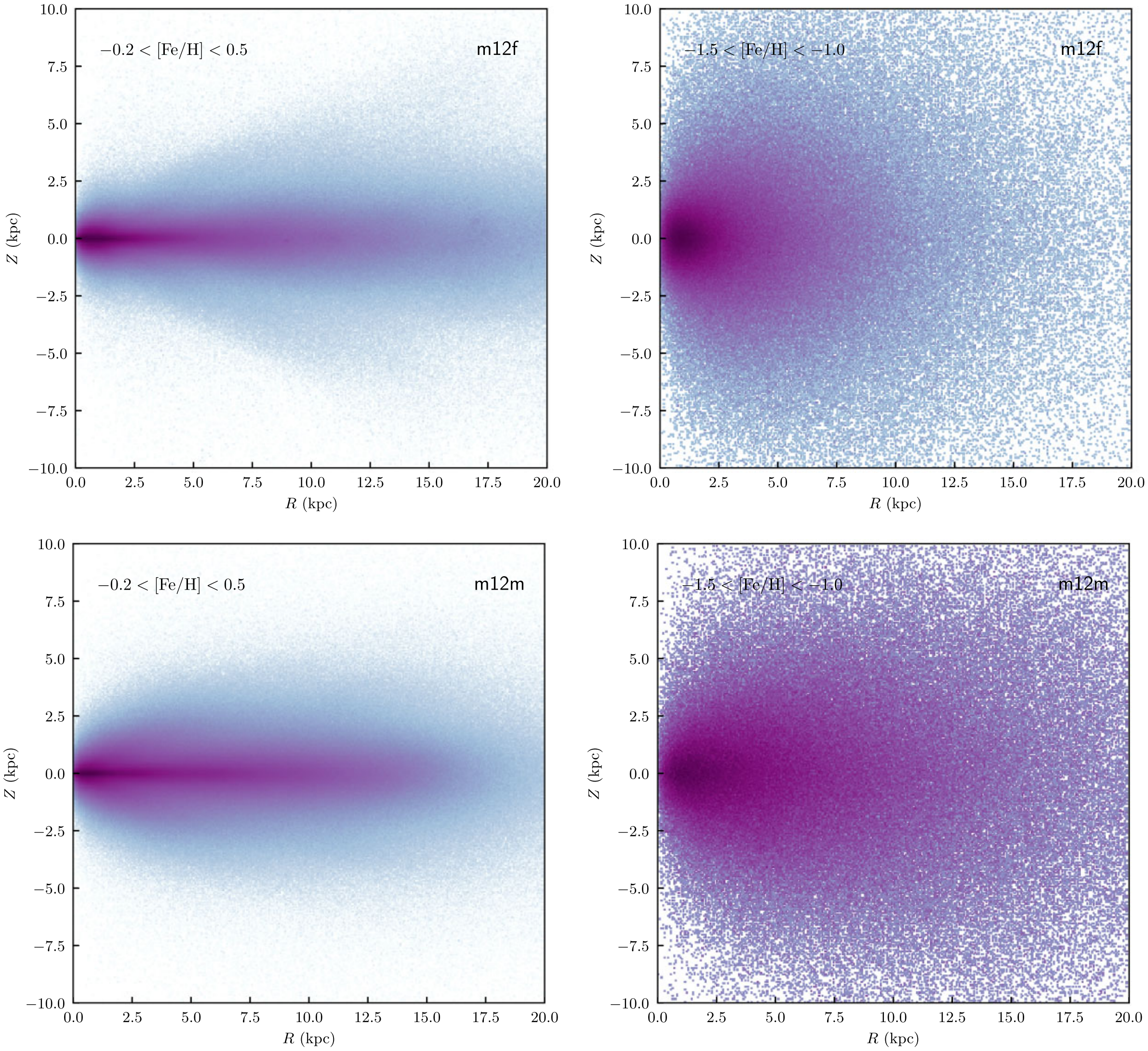

Figure A1. Distribution of the *in-situ* stellar particles at $z = 0$ of two MW-sized galaxies from the FIRE suite in the $Z - R$ plane, where Z is the distance from the plane of the disc defined as the plane perpendicular to the angular momentum of all stars and R is the galactocentric distance. The top row shows `m12f` object and bottom row shows `m12m`; the left-hand panels show stars with $-0.2 <$ [Fe/H] < 0.5 that form in the last several Gyrs and are distributed in a discy configuration, while the right-hand panels show metal poor stars with $-1.5 <$ [Fe/H] < -1 that form during earlier chaotic epochs which have a spheroidal distribution at the shown $z = 0$ epoch.

APPENDIX B: ASYMMETRY OF THE CHEMICAL ABUNDANCE DISTRIBUTION AT [FE/H] < −0.9

Fig. B1 gives $+1.65\sigma_{\mathrm{[X/Fe]}}$ ($-1.65\sigma_{\mathrm{[X/Fe]}}$) measured as the difference between the 95th and 5th (50th and 5th) percentiles of [X/Fe] distribution in dark (light) blue. These can be compared to 2 × the uncertainty of the abundance ratio measurement as a function of [Fe/H] shown as a dotted line in each panel. Interestingly, for several elements there exist ranges of [Fe/H] where the measured one-sided spread is as narrow as the measurement uncertainty. This confirms that while astonishingly low, the ADR17 abundance uncertainties, none the less, give a good representation of the quality of the measurement. At [Fe/H] > -0.9 the elements where a clear bifurcation at fixed metallicity is present, the $+1.65\sigma$ and -1.65σ curve exhibit distinct behaviour as the prominence of the upper and lower branches changes with [Fe/H]. For [Fe/H] < -0.3 the upper branch is more populated and thus contains the mode of the distribution, while the lower branch contributes to the -1.65σ spread. For [FeH] > -0.3, the branches switch and the bifurcation is reflected in $+1.65\sigma$ curve.[6]

---

[6] We do not discuss the difference between $+1.65\sigma$ and -1.65σ curves for [Al/Fe] since a selection cut is applied to this element restricting the lower wing of the distribution for the *in-situ* stars

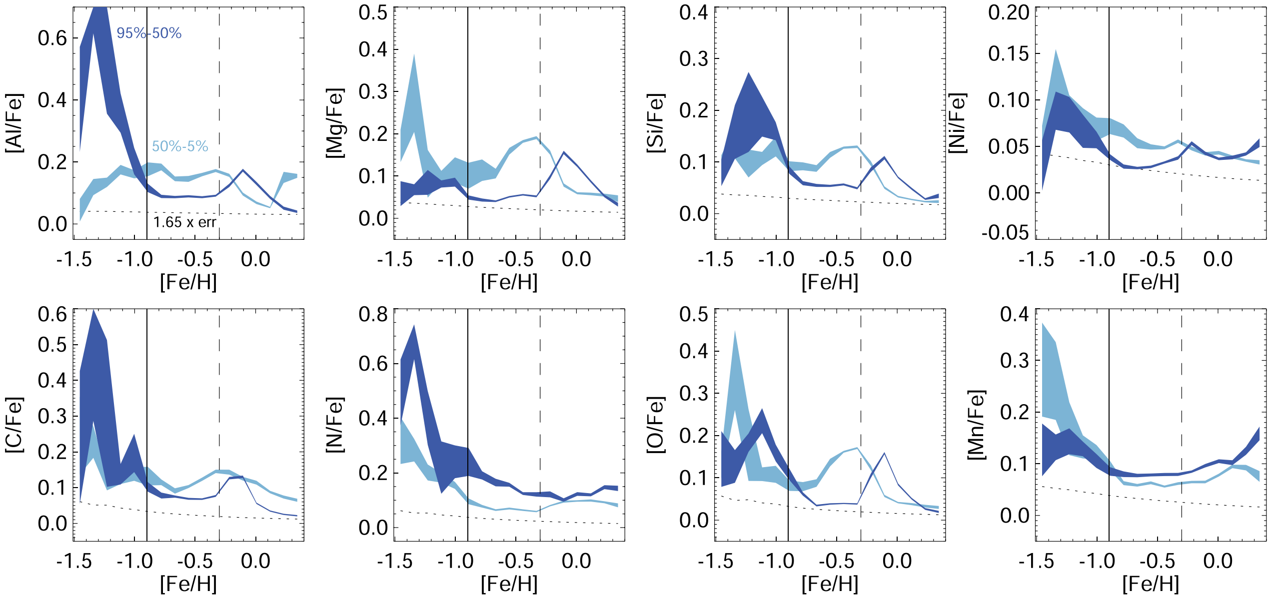

Figure B1. Asymmetry of the abundance distribution. For each element, positive (negative) excursion above median is shown as dark (light) blue band, corresponding to ±1.65$\sigma_{[\mathrm{X/Fe}]}$.

This paper has been typeset from a TEX/LATEX file prepared by the author.